Advancing Isotope-Enabled Model for Comprehensive Understanding of Atmospheric Sulfur Isotope Effects: ~~Revealing~~Demonstrating the Overlooked Isotopic Fractionation During Combustion and Flue Gas Desulfurization

Lianfang Wei[1,2,3], Xueshun Chen[1], Wenyi Yang[4], Zhe Wang[1], Jie Li[1], Di ~~Liu~~[1]Liu[5], Huiyun Du[1], Xiaole Pan[1], Yafang Cheng[3], Pingqing ~~Fu~~[5]Fu[6], Zifa Wang[1,~~6~~7]**

[1] State Key Laboratory of Atmospheric ~~Boundary Layer Physics~~Environment and ~~Atmospheric Chemistry~~Extreme Meteorology, Institute of Atmospheric Physics, Chinese Academy of Sciences, Beijing 100029, China

[2] Chinese Research Academy of Environmental Sciences, Beijing 100012, China

[3] Aerosol Chemistry Department, Max Planck Institute for Chemistry, Mainz, Germany

[4] Center of Air Quality Simulation and System Analysis, Chinese Academy of Environmental Planning, Beijing 100012, China

[~~5~~5] State Key Laboratory of Regional Environment and Sustainability, School of Environment, Beijing Normal University, Beijing 100875, China

[6] Institute of Surface-Earth System Science, School of Earth System Science, Tianjin University, Tianjin 300072, China

[~~6~~7] University of Chinese Academy of Sciences, Beijing, 100049, China

Corresponding author: Pingqing Fu (fupingqing@tju.edu.cn), Zifa Wang (zifawang@mail.iap.ac.cn)

样式定义: 正文
样式定义: 批注文字
样式定义: 批注框文本
样式定义: 页脚
样式定义: 页眉
样式定义: 普通(网站)
样式定义: Reference
样式定义: Heading-Main
样式定义: Text
样式定义: Figure or Table Caption
样式定义: Key Points
样式定义: EndNote Bibliography Title: 检查拼写和语法
样式定义: EndNote Bibliography: 检查拼写和语法
带格式的: 正文

Abstract

The isotopic composition of atmospheric species provides fundamental insights into their sources, sinks, and chemical processes. ~~However, conventional~~Conventional end-member mixing ~~box~~ models ~~fail to accurately represent the~~, however, cannot capture progressive isotopic evolution ~~within complex~~in open systems~~,~~ where mixing and ~~reactions occur~~reaction proceed simultaneously. This limitation hinders a comprehensive understanding of the isotope effect and its atmospheric applications. ~~To address this~~Here, we ~~have designed~~develop an ~~isotopic chemistry module and incorporated it into the three-dimensional~~ isotope-enabled chemical transport model~~, utilizing an iterative time-splitting method to mitigate the bias introduced by the Rayleigh equation. The model incorporates~~ (CTM) that tracks four sulfur isotopologues ($^{32}SO_2$, $^{34}SO_2$, $^{32}SO_4^{2-}$, $^{34}SO_4^{2-}$) ~~as prognostic tracers for~~ through emissions, transport, chemistry, and deposition. An iterative time-splitting method reduces the numerical bias from applying the Rayleigh equation in the open atmosphere. The model reproduces the ^{34}S enrichment of sulfate relative to SO_2 and ~~sulfate aerosol, simulating isotope effects during various gas-phase, heterogeneous/multiphase~~captures the spatial and ~~aqueous-phase reactions. Validation against compiled observation data demonstrates the model's ability to reproduce~~ seasonal patterns of the sulfur isotope effect ~~($\Delta\delta^{34}S\_SO_4^{2-}/SO_2$ = 3.43±1.11‰) and spatiotemporal variations of $\delta^{34}SO_4^{2-}$~~ across ~~Eastern~~eastern China~~.~~ (simulated $\Delta\delta^{34}S\ SO_4^{2-}/SO_2$ = 6.11±1.85‰; observed = 3.43±1.11‰). Further, ~~our study underscores~~the agreement between simulated (with $\delta^{34}S\ SO_2$ = 0‰ emission assumption) and observed sulfate isotopic compositions, combined with the documented higher $\delta^{34}S$ values of coal at 1‰–10‰ across eastern China, implies a systematic ^{34}S depletion in emitted SO_2 relative to fuels. This highlights the importance of considering isotopic fractionation during combustion, flue gas desulfurization and chemical processes for accurate source apportionment ~~using the isotope mixing model.~~. The isotope-enabled model ~~presents an innovative~~provides a new approach for ~~effectively~~ constraining the sulfur budget.

Graphical Abstract

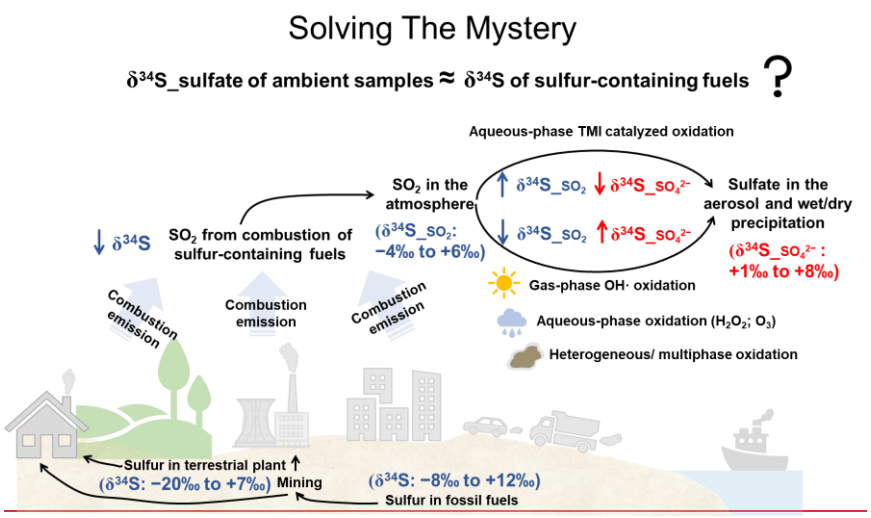

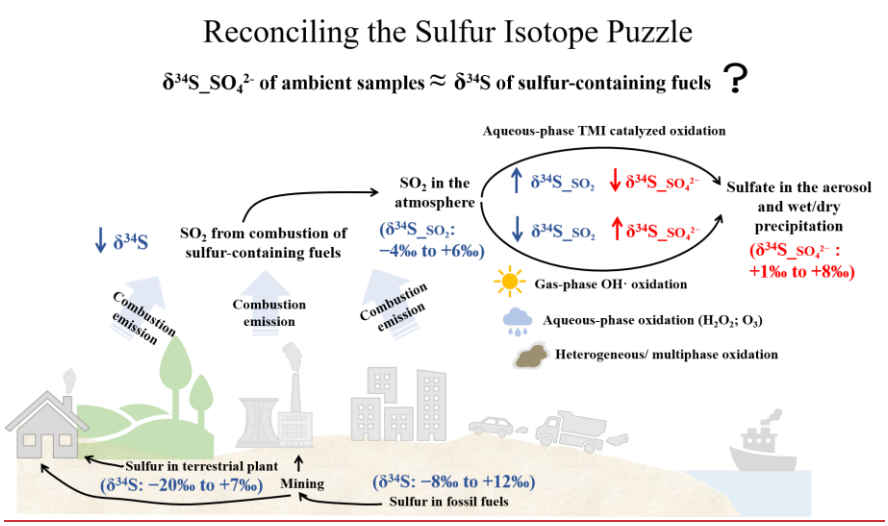
Reconciling the Sulfur Isotope Puzzle
δ34S_SO4 2- of ambient samples ≈ δ34S of sulfur-containing fuels ?
Aqueous-phase TMI catalyzed oxidation
SO2 in the atmosphere
(δ34S_SO2: −4‰ to +6‰)
δ34S_SO2
δ34S_SO4 2-
δ34S_SO2
δ34S_SO4 2-
Sulfate in the aerosol and wet/dry precipitation
(δ34S_SO4 2- : +1‰ to +8‰)
δ34S
SO2 from combustion of sulfur-containing fuels
Gas-phase OH· oxidation
Aqueous-phase oxidation (H2O2; O3)
Heterogeneous/ multiphase oxidation
Combustion emission
Combustion emission
Combustion emission
Sulfur in terrestrial plant
(δ34S: −20‰ to +7‰)
Mining
(δ34S: −8‰ to +12‰)
Sulfur in fossil fuels

1 Introduction

Sulfate and sulfur dioxide (SO_2) have complex interactions with the environment and Earth's climate system, involving aerosol and cloud formation, climate cooling, and the global sulfur budget ~~(Seinfeld and Pandis, 2016).~~(Seinfeld and Pandis, 2016). The primary sources of SO_2 emissions are from the combustion of sulfur-containing fuels (coal and oil, etc.) at power plants, industrial facilities, and residential heating (Crippa et al., 2023). The atmospheric oxidation of SO_2 to sulfate has been extensively investigated through gas-phase reactions with OH radicals and heterogeneous/multiphase oxidation involving H_2O_2, O_3, NO_2, and transition metal ion catalysis (TMI-catalysis).

Recent investigations into sulfate isotopic composition have emerged as promising proxies for gaining fundamental insight into the sulfate's sources, sinks, and concentration-independent information on atmospheric oxidation processes. However, there remains a significant discrepancy among studies that use the end-member mixing model. Han et al~~.~~. (2016a) emphasized the dominance of biological sulfur emissions in summer and coal combustion in winter. Lin et al~~.~~. (2022) illustrated how isotopic fractionation significantly reshapes the sulfur isotopic composition in sulfate, leading to distinctive results of source apportionment. While Feng et al~~.~~. (2023) highlighted the impact of sulfur isotopic fractionation during combustion on source apportionment, identifying traffic emissions (49%) and coal combustion (46%−65%) as major contributors to sulfate during heavy pollution in the North China Plain. Discrepancies also arise in identifying the dominant SO_2 oxidation pathway. Fan et al~~.~~. (2020) highlighted SO_2 oxidized by NO_2 and TMI-catalyzed O_2 as a key contributor to high sulfate loading using $\delta^{34}S\_SO_4^{2-}$. While Han et al~~.~~. (2022) revealed enhanced SO_2 oxidation by H_2O_2, supported by $\delta^{34}S$~~-~~_SO_2 and $\delta^{34}S\_SO_4^{2-}$ analyses. Several limitations may explain these divergences. (1) Studies rely on the Rayleigh distillation equation, which is only suitable for closed systems with reservoir-limited conditions, leading to an increasing apparent isotope effect as the reservoir is progressively consumed (Guan and Liu, 2023). (2) Laboratory studies have indicated that the combustion process, atmospheric chemistry and mixing can reshape the sulfur isotopic composition from the sources of sulfur-containing fuels to SO_2 and sulfate.

Therefore, our goal is to reconcile the ongoing debate among previous research findings related to sulfur isotope tracing and establish a comprehensive understanding of the atmospheric isotope effect. To achieve this, developing an isotope-enabled model that integrates isotopic chemistry and the isotopic fingerprints of emission sources is crucial. Recent applications have incorporated isotope effects into ~~chemical transport models (~~CTMs~~)~~ to simulate $\delta^{15}N$ of atmospheric NO_x and NO_3^- using CMAQ (Fang and Michalski, 2022) and mercury isotopic fractionation using GEOS-Chem (Song et al., 2022). These methodologies involve using isotopologues as prognostic tracers and scaling the rate constants of different isotopologues with their corresponding isotope fractionation factor. However, these models primarily focus on "gas-phase" or one-step unidirectional kinetic reactions. ~~Considering the complexity of sulfur~~Sulfur chemistry~~, which~~ involves heterogeneous and multiphase reactions with ~~several processes, including~~ mass transfer, dissociation equilibrium, and chemical reaction. ~~It is extremely difficult and challenging to determine the~~Determining reaction intermediates and their isotopic fractionation ~~factor~~factors for each elementary step is therefore challenging. In addition, the isotope effects obtained from laboratory studies for complex reactions

设置了格式

设置了格式

represent apparent or overall isotope effects. Consequently, the incorporation of isotopic chemistry into CTMs faces new challenges, especially with heterogeneous/multiphase reactions.

In this study, we develop a ~~newly~~new isotope-enabled model to simulate the isotopic compositions of sulfur-bearing species, considering both physical mixing and isotopic fractionation due to chemical reactions, and enabling the explicit simulation of progressive depletion/enrichment in the reservoir and their impact on sulfate production. The study aims to present a comprehensive description of the isotope-enabled model, evaluate its skill in reproducing the spatial-temporal variations in sulfur isotope composition, and ~~enhance a comprehensive~~deepen our understanding of the atmospheric sulfur isotope effects.

2 Methodology

2.1 Model framework

We incorporate the isotopic chemistry module into the Eulerian atmospheric chemistry transport models NAQPMS. The NAQPMS is a Nested Air Quality Prediction Model System developed by the Institute of Atmospheric Physics (IAP), Chinese Academy of Sciences (CAS) (Wei et al., 2019; Chen et al., 2021; Wang et al., 2001), including physical processes (advection, diffusion, and dry/wet deposition), chemistry module (gas and aqueous chemistry, aerosol chemistry and thermodynamics, and mercury chemistry) (Chen et al., 2015), and online emission of dimethyl sulfide, sea salt, and dust. The Advanced Particle Microphysics module (APM) and 1.5-D Volatility Basis Set (VBS) aerosol schemes are also coupled to simulate the aerosol microphysical processes and organic aerosol formation, respectively (Chen et al., 2019; Yang et al., 2019; Chen et al., 2014).

The simulation is performed with a two-way nested configuration. The external domain D1 covers the mainland of China at a horizontal resolution of 45 km, while the innermost domain D2 is centered over eastern China with a finer resolution of 15 km, as illustrated in Figure 1. The model runs on 20 atmospheric vertical layers, utilizing terrain-following hybrid sigma coordinates from the surface to an altitude of 20 km. The sulfur chemistry from SO_2 to S(VI) involves gas, heterogeneous and aqueous-phase oxidation. The gas-phase chemistry incorporates the Carbon Bond Mechanism Z (CBM-Z) (Zaveri and Peters, 1999). For aqueous chemistry, the Regional Acid Deposition Model (RADM2) is applied, resolving cloud-phase sulfur oxidation through dissoluble S(IV) with O_3, H_2O_2, proxy acetic acid (CH_3OOH), and transition metal-catalyzed O_2 (Stockwell et al., 1997). The oxidation of S(IV) species by dissolved NO_2 is also incorporated into the sulfur aqueous chemistry, referring to the kinetic parameters proposed by Cheng et al.(2016). Heterogeneous reactions of SO_2 on various surfaces, including dust, sea salt, soot and deliquesced aerosols, have also been incorporated using the reactive uptake coefficients parameterization (Li et al., 2018). The gas-particle partitioning of inorganic aerosols and aerosol water content are simulated using the improved ISORROPIA II (Fountoukis and Nenes, 2007; Song et al., 2018). The simulation began in March 2014. The initial 3 months

设置了格式

~~serve~~served as a spin-up time. For additional details on the model and its detailed configuration, refer to Text S1 and Table S2.

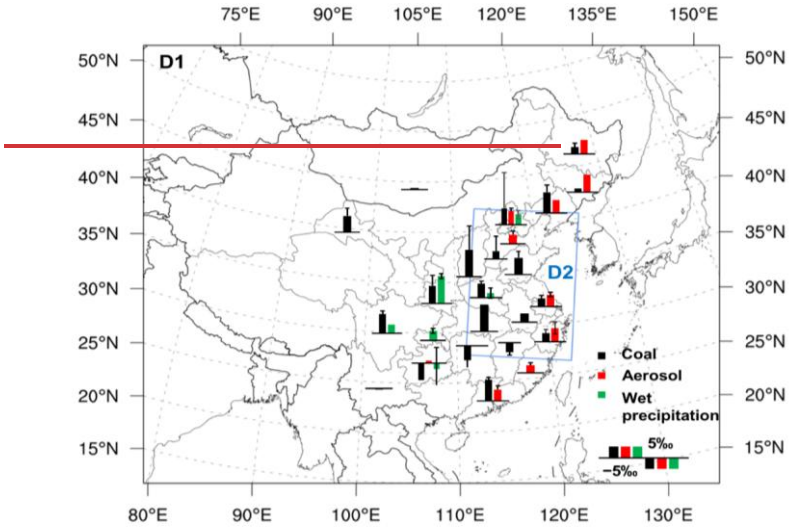

~~Figure 1.~~ ~~Simulation domains with nested modeling. D1 and D2 represent the parent and child domains, respectively. Overlaid bar graphs with error bars illustrate compiled sulfur isotopic composition ($\delta^{34}S$) data from coal, aerosols, and precipitation across different regions in China.~~

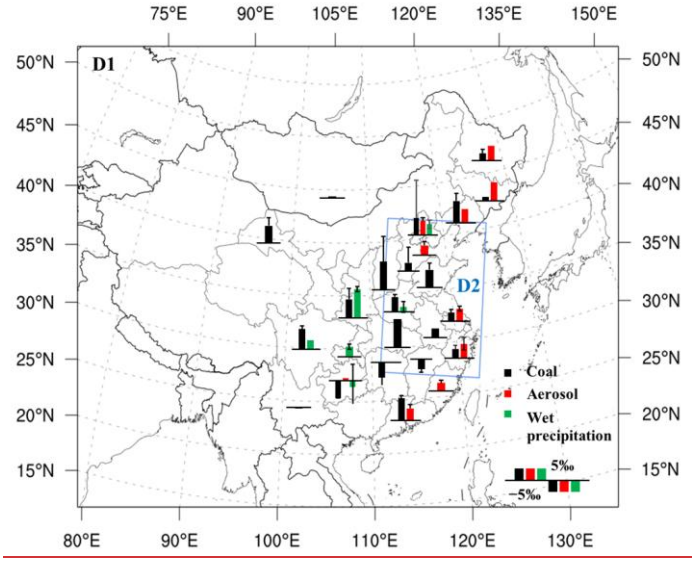

Figure 1. Model domain and compiled sulfur isotopic composition ($\delta^{34}S$) data. The simulation uses a two-way nested configuration, with the parent domain D1 covering the Chinese mainland (45 km resolution) and the child domain D2 centered over eastern China (15 km resolution). Literature-reported $\delta^{34}S$ data are overlaid at sampling locations. Black, red, and green bars denote the mean ± one standard deviation of $\delta^{34}S$ of coal, aerosol sulfate, and wet precipitation sulfate, respectively. The small black bar near Inner Mongolia denotes coal $\delta^{34}S$ value only (regional mean = 0.8‰), no aerosol or wet precipitation sulfate $\delta^{34}S$ are available there. All values are in per mil (‰). Additional details on the observed data can be found in Table S1.

2.2 Isotope notation and isotopic fractionation

The sulfur element is widely present throughout all natural environments and possesses four stable isotopes, namely ^{32}S, ^{33}S, ^{34}S, and ^{36}S, with relative abundances of 95.02%, 0.75%, 4.21%, and 0.02%, respectively (De Laeter et al., 2003). In general, the sulfur isotopic composition is denoted as $\delta^{x}S$ value in per mil (‰), where ^{x}S represents one of the less abundant isotopes, e.g., ^{33}S, ^{34}S, or ^{36}S~~).~~. This notation is defined as the difference between the isotopic ratio of a given sample and the reference standard V-CDT (Vienna Canyon Diablo Troilite):

$$\delta\,{}^{x}S_{Sample}(‰) = \left(\frac{R({}^{x}S/{}^{32}S)_{Sample}}{R({}^{x}S/{}^{32}S)_{V-CDT}} - 1\right) \times 1000 \quad (1)$$

Where R represents the isotopic ratio, ~~as~~ defined as the atomic abundance ratio of ~~any minor~~heavier to ~~a major abundant~~lighter stable isotope, expressed as $R(\_^{x}S/\_^{32}S) = \frac{N(\_^{x}S)}{N(\_^{32}S)}$.= $N(\,{}^{h}X)/N(\,{}^{l}X)$, where $N(\,{}^{h}X)$ and $N(\,{}^{l}X)$ represent the atomic abundances of the heavier stable isotope ($\,{}^{h}X$) and lighter stable isotope ($\,{}^{l}X$), respectively. V-CDT is the international sulfur isotope standard, with isotopic ratios of $R(^{34}S/^{32}S)_{V\text{-}CDT}$= 0.044163 and $R(^{33}S/^{32}S)_{V\text{-}CDT}$ = 0.007877 (Ding et al., 2001).

Isotope ~~effect~~effects are observable in physical or chemical processes, especially during equilibrium (or thermodynamic) and kinetic processes, leading to ~~changed~~a change in isotope distribution between two substances or different phases of the same substance with distinct isotope ratios. Isotopic fractionation is often a result of the isotope effect. The isotopic fractionation factor $\alpha\,{}^{h}X_{P/S}$ is defined as the ratio of isotopic ratio of the instantaneously formed product ~~$R(\_^{h}X/\_^{l}X)_{Pi}R_{Pi} = (N(\,{}^{h}X)/N(\,{}^{l}X))_{Pi}$~~ and substrate ~~$R(\_^{h}X/\_^{l}X)_{S}R_S =$~~ $(N(\,{}^{h}X)/N(\,{}^{l}X))_{S}$ (Mariotti et al., 1981),

$$\alpha\,{}^{h}X_{P/S} = \frac{R(\_^{h}X/\_^{l}X)_{Pi}}{R(\_^{h}X/\_^{l}X)_{S}} = \frac{R_{Pi}}{R_S} \quad (2)$$

For thermodynamic (equilibrium) or unidirectional kinetic process with a single-step reaction following a first-order rate law, the $\alpha\,{}^{h}X_{P/S}$ can be interpreted as the ratio of rate constant *k* or equilibrium constant *K*:

$$\alpha\,{}^{h}X_{P/S} = {}^{h}k/{}^{l}k = {}^{h}K/{}^{l}K \quad (3)$$

An isotope enrichment factor, ε (in per mil ‰), can be defined as:

带格式的: 居中

带格式的: 居中

带格式的: 居中

$$\varepsilon = (\alpha\alpha\ {}^{h}X_{P/S} - 1) * 1000 \quad (4)$$

The $\alpha\alpha\ {}^{h}X_{P/S}$ determines how much faster or slower the reaction with the minor/heavyheavier isotopologues proceeds relative to the reaction with the major/lightlighter isotopologues.

Generally, isotopic fractionation determined in laboratory experiments represents overall isotope effects, resulting from physical, equilibrium, and kinetic fractionation. The isotopic composition between reservoir and product, as a function of reactant extent and fractionation factor, is described by the Rayleigh fractionation equations. Taking the example of the isotopic effect of gas- and aqueous-phase oxidation of SO_2, the Rayleigh equations describe the process as:equation.

$$R(\ {}^{h}\_X/\ {}^{l}\_X)_{S_t}/R(\ {}^{h}\_X/\ {}^{l}\_X)_{S_0} = f_{rem}^{(\alpha^{\ {}^{h}\_X_{P/S}} - 1)} \quad (5)$$

$$R_{S,t}/R_{S,t0} = f_{rem}^{(\alpha^{\ {}^{h}X_{P/S}} - 1)} \quad (5)$$

where f_{rem} is the fraction of residual reactant SO_2, $R(\ {}^{h}\_X/\ {}^{l}\_X)_{S_0}$, $R_{S,t0}$ and $R(\ {}^{h}\_X/\ {}^{l}\_X)_{S_t}$ $R_{S,t}$ are the isotope ratio $^{34}S/^{32}S$ of substrate at initial and remaining reactant at t_0 and t moment, respectively. The instantaneous isotope ratio of the product $(R(\ {}^{h}\_X/\ {}^{l}\_X)_{P_t})R_{P,t}$ at t moment is given by:

$$R(\ {}^{h}\_X/\ {}^{l}\_X)_{P_t}/R(\ {}^{h}\_X/\ {}^{l}\_X)_{S_0} = \alpha f_{rem}^{(\alpha^{\ {}^{h}\_X_{P/S}} - 1)} \quad (6)$$

The average isotope ratio of accumulated product $(\overline{R(\ {}^{h}\_X/\ {}^{l}\_X)_P})$ during the reaction can be derived from the isotope mass balance:

$$\overline{R(\ {}^{h}\_X/\ {}^{l}\_X)_P}/R(\ {}^{h}\_X/\ {}^{l}\_X)_{S_0} = \frac{1 - f_{rem}^{(\alpha^{\ {}^{h}\_X_{P/S}} - 1)}}{1 - f_{rem}} R_{P,t}/R_{S,t0} = \alpha^{\ {}^{h}X_{P/S}} \times f_{rem}^{(\alpha^{\ {}^{h}X_{P/S}} - 1)} \quad (6)$$

The average isotope ratio of accumulated product ($\overline{R_P}$) during a finite reaction interval follows the standard Rayleigh-fractionation expression for accumulated products (Hoefs, 2015):

$$\overline{R_P}/R_{S,t0} = \frac{1 - f_{rem}^{(\alpha^{\ {}^{h}X_{P/S}} - 1)}}{1 - f_{rem}} \quad (7)$$

2.3 Developing Isotope-Tagged Emission Inventories

The multi-resolution Emission Inventory for China (MEIC, http:// http://meicmodel.org.cn/?p=1579&lang=en) provides a comprehensive SO_2 emission inventory, including anthropogenic emissions from power plants, industry, residential, and transportation, respectively. Primary combustion sulfate, which forms as the oxidation product in the chimney and plumes (Sun et al., 2023; Ding et al., 2021), is assumed to be 5%wt of anthropogenic SO_2 (Berglen et al., 2004). Anthropogenic sulfur-containing sources exhibit a highly variable and overlapping isotopic composition, ranging from −30‰ to 30‰ (Hoefs and Harmon, 2022). We adopt a constant signature of $\delta^{34}S$= 0‰ V-CDT for anthropogenic SO_2 emission sources.

带格式的: 居中

设置了格式: 非上标/ 下标

带格式的: 居中

~~Consequently, direct comparisons between simulated and observed $\delta^{34}SO_2$ and $\delta^{34}SO_4^{2-}$ values are not available. However, the~~This simplification isolates the atmospheric chemical isotope effect from poorly constrained source signatures.

The sulfur isotope difference between SO_2 and sulfate (~~$\Delta^{34}S$~~$\Delta\delta^{34}S\_SO_4^{2-}/SO_2 = \delta^{34}S\_SO_4^{2-} - \delta^{34}S\_SO_2$~~), approximating~~) approximates the ~~value of~~ apparent isotopic fractionation multiplied by 1000~~‰,~~‰ and is hereafter referred to as the isotope effect~~,~~. $\Delta\delta^{34}S\_SO_4^{2-}/SO_2$ is mathematically independent of the absolute emission $\delta^{34}S$ and can be ~~applied to~~therefore validate the oxidation module of isotope-enabled ~~CTMs.~~ CTM. By contrast, the $\delta^{34}S\_SO_2$ and $\delta^{34}S\_SO_4^{2-}$ depend on the prescribed emission signature. Direct comparisons between simulated and observed $\delta^{34}S\_SO_2$ and $\delta^{34}S\_SO_4^{2-}$ are subject to the uncertainties of this assumption and should be interpreted with caution. Jointly examining the simulated and observed $\delta^{34}S\_SO_2$ and $\delta^{34}S\_SO_4^{2-}$ together with $\Delta\delta^{34}S\_SO_4^{2-}/SO_2$ provides a diagnostic of whether a given model–observation bias arises primarily from the atmospheric oxidation processes or from the assumed emission-source signatures.

The tracer mass of $^{32}SO_2$, $^{34}SO_2$, $^{32}SO_4^{2-}$, $^{34}SO_4^{2-}$ isotopologues can be determined from the SO_2 mass in the emission inventory based on the Equation (1), with the initial values of R~~$R(^{34}S/^{32}S)_{V-CDT}$~~R_{V-CDT} at 0.044163.

$$^{34}S = {}^{32}S \times \left(\left(\frac{\delta^{34}S}{1000} + 1\right) \times ~~R(^{34}S/^{32}S)_{V-CDT}~~ R_{V-CDT}\right) \quad (8)$$

带格式的: 居中

2.4 Coupled methodology of isotopic chemistry module

2.4.1 The development of isotopic chemistry module

To dynamically simulate the spatiotemporal distribution of isotopic composition ($\delta^{34}S$) in particle SO_4^{2-} and its gaseous precursor SO_2, we have implemented the tagging technology and isotopic chemistry module into the atmospheric chemistry transport model. The four isotopologues ($^{32}SO_2$, $^{34}SO_2$, $^{32}SO_4^{2-}$, $^{34}SO_4^{2-}$) are treated as independent prognostic tracers of SO_2 and sulfate aerosol throughout their entire atmospheric life cycle, including emission, transport, chemical production/loss, and deposition processes.

Generally, ~~the~~ previous isotope-enabled models incorporating isotope chemistry typically only consider kinetic isotope fractionation, deriving different rate coefficients for individual isotopologues from isotopic fractionation factors (α) with Equation (4) (Fang and Michalski, 2022; Gromov et al., 2010). This assumption is suitable for single-step, steady-state reactions, such as gas-phase chemical reactions. However, most processes in natural systems involve reaction sequences; each reaction within the sequence exhibits its intrinsic isotope fractionation, and not all isotope fractionation of these individual reactions is measurable. For example, the cloud and aqueous-phase chemical module ~~involves~~involve gas-to-particle equilibrium, dissolution, diffusion, and chemical reactions. Thus, the isotope effect observed in the complex system with multiple intermediates represents an overall isotope effect. If the reaction sequences have a given end product, the conventional approach for deriving the isotope effect requires ~~the~~ repeated determination of ~~$R_{s,0}$, R_p,~~ $R_{S,t0}$, $\overline{R_P}$ and ~~f in a closed~~

system. f_{rem}. The isotope fractionation factor is then calculated using the Rayleigh equations with the isotope ratio or "δ" value,equation as,

$$R_p = R_{s,0} \times \frac{1-f^{\alpha_{p/s}}}{1-f} \quad (9)$$

$$\delta_p \approx \delta_{s,0} - \varepsilon \times \frac{f \times \ln(f)}{1-f} \quad (10)$$

$$\overline{R_P} = R_{S,t0} \times \frac{1-f_{rem}^{(\alpha^{\ h}X_{P/S}-1)}}{1-f_{rem}} \quad (9)$$

When a substrate is consumed through multiple competing pathways simultaneously, the Rayleigh equation relates the change in the isotopic ratio of substrate to the extent of substrate consumption, employing the apparent overall isotopic fractionation factor (α_A) (Van Breukelen, 2007). The factor of α_A is expressed as a function of various instantaneous isotopic fractionation factors (α_{ins}) associated with individual pathways, given by the following equation:

$$\alpha_A = F_1 \times \alpha_{ins\_1} + F_2 \times \alpha_{ins\_2} + \ldots + F_n \times \alpha_{ins\_n} \quad (10)$$

带格式的: 居中

Where F_i is the ratio of contribution from the *i*-th process to the overall product.

Therefore, the $^{34}S/^{32}S$ sulfur isotopic ratio of the residual SO_2 within the grid cell can be determined using the following equation:

$$R(^{34}S/^{32}S)_t = R(^{34}S/^{32}S)_{t_0} \times f_{rem} \times exp(\alpha_A - 1) = R(^{34}S/^{32}S)_{t_0} \times f_{rem} \times \exp[(\Sigma F_i \times \alpha_{ins\_i}) - 1]$$

$$R_{S,t} = R_{S,t0} \times f_{rem}^{\ (\alpha_A - 1)} = R_{S,t0} \times f_{rem}^{\ (\sum F_i \times \alpha_{ins\_i} - 1)} \quad (11)$$

To directly apply the measured isotopic isotope fractionation from factors measured in laboratory studies, we have developed an independent isotopic chemistry module utilizingcoupled to the host CTM, as illustrated in Figure 2. The module utilizes Rayleigh equation fractionation equations to solve thecalculate isotopologues changechanges between reactants and products. This module tracks the net change in , combined with the iterative time-splitting method described in Section 2.4.2 to reduce numerical bias. At each model time step, the module receives SO_2 loss and sulfate based on outputproduction separately from the gas-phase, heterogeneous, and cloud&/aqueous-phase chemistry modules separately, and then the relative contribution of specificeach oxidation pathwayspathway is calculated and recorded. It Temperature-dependent isotope fractionation factors are then updated in each grid cell according to the local temperature. The module tracks the net changes in four isotopologues ($^{32}SO_2$, $^{34}SO_2$, $^{32}SO_4^{2-}$, $^{34}SO_4^{2-}$) and updates the temperature-dependent isotopic fractionation factor in the specific grid cell and calculates the net isotopologue changetheir concentrations through an iterative time-splitting procedure, which divides each oxidation calculation into smaller SO_2 conversion sub-steps. Within each sub-step, isotope ratios are calculated using Rayleigh fractionation equations and, isotopic mass balance. The is enforced, and the isotopic composition of the reactant reservoir and accumulated product is updated. The full algorithm framework is depicted in Figure 2 and described in further documented in Text S2.

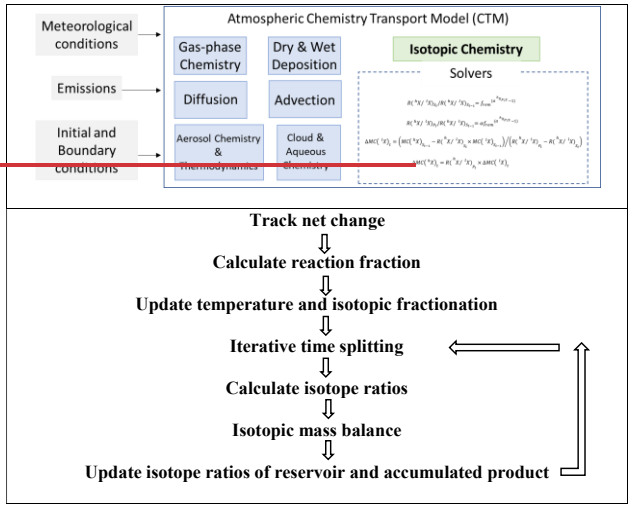

~~**Figure 2.** The algorithm framework to calculate the net isotopologue change at every time step.~~

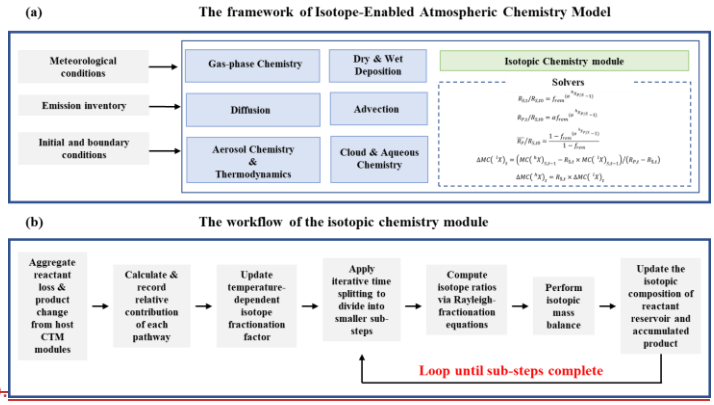

Figure 2. Algorithmic framework of the isotope-enabled CTM and the isotopic chemistry module. (a) Host CTM framework, including the main physical and chemical modules (gas-phase chemistry, aerosol chemistry and thermodynamics, cloud and aqueous chemistry, advection, diffusion, and dry and wet deposition) and their coupling with the isotopic chemistry module. (b) The workflow of the isotopic chemistry module. At each time step, the module tracks net SO_2 and sulfate changes, calculates reaction fractions, updates temperature-dependent fractionation factors, applies iterative time splitting, computes isotope ratios via Rayleigh-fractionation equations, performs isotopic mass balance, and updates the isotope ratios of the reactant reservoir and accumulated product.

设置了格式: 字体: +西文正文 (Calibri)

Based on the assumptions outlined in Text S1, the $\delta^{34}S$ is primarily influenced by fractionation during different chemical reactions. Relevant sulfur isotopic fractionation data have been sourced from laboratory studies conducted by Harris et al. (Harris et al., 2012b; Harris et al., 2012c; Harris et al., 2012a; Harris et al., 2013), including the gas-phase oxidation by OH radicals, aqueous-phase oxidation by H_2O_2, O_3, and iron catalysis, heterogeneous oxidation of SO_2 on sea salt aerosol and mineral dust (see Table 1). The sulfur isotopic fractionation during SO_2 oxidation by NO_2 in the aqueous phase, as determined by Yang et al. (2018), is excluded from this study. This exclusion is attributed to their methodology, which yielded an apparent isotopic fractionation factor calculated by dividing the isotopic ratio of accumulated production by the initial isotope ratio of reactant. This calculation assumed that R_{pi} was approximated by ~~R_p with f being approximately 1. However, an error in the calculation with this approximation is estimated to fall between 0.5‰ and 3‰, with f ranging from 0.9 to 0.95 (Toyoda et al., 2005).~~ $\overline{R_p}$ with f_{rem} being approximately 1. This approach contrasts with the conventional definition of the isotope fractionation factor, which typically represents the isotope ratio in the instantaneously formed product in an infinitely short time divided by that of the reactant (Equation (2)) (Harris et al., 2013; Hoefs, 2015; Mariotti et al., 1981). For reference in our discussion, the apparent isotopic fractionation factor $\alpha^{34}S_{NO2}$ (T at 3~~℃)~~ °C) = 0.998 is adopted in the simulation.

Table 1. The sulfur isotopic fractionation factor determined by the lab experiment and its temperature dependency for a specific oxidation pathway.

Oxidation pathway	Reaction Type	Symbol	Model isotope fractionation factor α (at 0~~℃)~~ °C)	T dependence ~~(-℃-~~(°C^{-1})	Reference
S(IV)+OH·	Gas-phase	$\alpha^{34}S_{OH}$	1.0106	-0.004	(Harris et al., 2012c)
S(IV)+H_2O_2	Aqueous-phase	$\alpha^{34}S_{H2O2}$	1.0165	-0.085	(Harris et al., 2012c)
S(IV)+O_3	Aqueous-phase	$\alpha^{34}S_{O3}$	1.0167	-0.085	(Harris et al., 2012c)
S(IV)+O_2 (TMI catalyzed)	Aqueous-phase	$\alpha^{34}S_{TMI}$	0.9949	-0.237	(Harris et al., 2013)
S(IV)+O_2 (TMI catalyzed)	~~on~~On mineral dust	$\alpha^{34}S_{TMI\_surface}$	1.0096 (T =19~~℃)~~ °C)	-	(Harris et al., 2012b)
S(IV)+O_3	On the ~~seasalt~~sea salt	$\alpha^{34}S_{seasalt}$	1.0124 (T =19~~℃)~~ °C)	-	(Harris et al., 2012a)

设置了格式

设置了格式: 字体: +西文正文 (Calibri)

设置了格式: 字体: Times New Roman

设置了格式: 字体: Times New Roman

设置了格式

设置了格式

$S(IV)+NO_2$	Aqueous-phase	$\alpha^{34}S_{NO2^-}$*	0.998 (-T =3℃) °C)	-	(Yang et al., 2018)

We consider the temperature dependence of the isotopic fractionation factor by utilizing the real-time temperature of the grid cell, thus avoiding a significant effect on the seasonal simulation of isotopic composition.

* $\alpha^{34}S_{NO2}$* denotes the apparent isotopic fractionation factor during SO_2 oxidation by NO_2 in the aqueous phase at 3℃, °C, $\alpha^{34}S_{NO2}$ (T at 3℃) °C) = 0.998±0.00041, was determined by Yang et al. (2018). In their laboratory experiment, SO_2 was oxidized by NO_2 in a reaction chamber containing liquid water. The isotopic composition $^{34}S\delta^{34}S$ in the initial SO_2 and accumulated sulfate product after 2 hours of reaction time was collected and measured. However, the residual fraction of SO_2 wasn'twas not measured, and the apparent isotopic fractionation factor was calculated by dividing the isotopic ratio of accumulated production by the ratio of reactant. As the reaction progresses, the isotopic composition of the accumulated product changes. Once the reactants are completely consumed, the isotopic composition of the accumulated product is equal to the initial reactants (See Figure 3). Therefore, according to the isotope mass balance, the apparent isotopic fractionation factor is highly dependent on the residual fraction during the reaction process, and cannot be equal to the exact isotopic fractionation factor, which is represented by the isotope ratio in the instantaneously formed product divided by the ratio in the reactant. Although the detected apparent isotopic fractionation factor can indicate the direction of isotopic fractionation (enrichment or depletion in the product relative to the reactant), it cannot be directly used in the model to calculate the isotope effect of $S(IV)+NO_2$ pathway.

设置了格式: 字体: +西文正文 (Calibri)

设置了格式: 字体: +西文正文 (Calibri)

2.4.2 Improving isotopic chemistry simulation with the iterative time-splitting method

In Chemical Transport Models (CTMs),CTM, numerical integration is crucial for solving the kinetic equations associated withof chemical mechanisms. In the gas-phase mechanism module, the CBMZ mechanism is coupled with the LSODES numerical solver (the sparse version of the Livermore ODE solver) to numerically solve ordinary differential equations representingintegrate the chemical transformations and provide species concentration changes in species concentrations over time. WhenIn the cloud and aqueous chemistry module is called, the distribution between gas and aqueous phasespartitioning is determined by instantaneous Henry'sHenry's law equilibrium. At; at each time step, thea bisection method is employed to estimateestimates pH and the distribution of ionic species, assumingspeciation under electroneutrality and thermodynamic equilibrium. The, and a forward Euler solver is used for the numerical integration of integrates the aqueous-phase sulfur oxidation reactions, with time stepping based on the reaction rates and precursor/oxidant concentrations for sulfate production alone. At the end of each incremental oxidation step, the chemical equilibrium will be reestablished. after each incremental oxidation step.

The classical Rayleigh distillation equation assumes that (i) the product, once formed, is immediately and irreversibly removed with no further isotopic exchange, and (ii) the reservoir receives no external input, the reactants being consumed solely by the fractionating reaction.

These assumptions do not hold in the open atmosphere ~~continuum involves simultaneous~~. Within a single integration step (~30 min), the reactant reservoir in each grid cell is continuously influenced by emissions, advection, and diffusive mixing. Because mixing and fractionation ~~processes. However, the Rayleigh equation has limitations as it assumes that a system that only experiences the loss of reactant without fresh mixture. When~~occur simultaneously, applying the Rayleigh equation ~~is employed in~~over the full-time step, especially under a large conversion fraction, makes the isotopic ~~chemistry module, the isotope~~ composition ~~of the product and remaining reactant highly depends on~~ sensitive to the residual fraction ~~of reactants~~ f_{rem}, which ~~is influenced by the~~ itself depends on time discretization and reaction ~~-~~rate constants. This artificially amplifies the apparent enrichment or depletion in the residual reactant, producing the so-called reservoir effect. Mitigating this bias provides the numerical motivation for the iterative time-splitting method used here.

~~In our simulation, we use a default time step of 30 minutes. Therefore~~To reduce the numerical bias that can arise when the Rayleigh equation is applied directly over a finite CTM time step in an open atmospheric system, we introduce an iterative time-splitting method ~~to effectively solve the problem arising from the effect of time discretization and reaction extent on the results calculated by Rayleigh equations. We also derive an equation with a precise integration method~~that divides each oxidation calculation into smaller conversion sub-steps and updates the isotopic composition iteratively. Within each main time step, the total reactant supplied by emissions, advection, and mixing is apportioned across the sub-steps. At the start of each sub-step, the reactant concentration and isotope ratio are updated by incorporating the freshly allocated reactant, after which the Rayleigh equation is applied under the approximately closed conditions of that sub-step, where the conversion fraction is kept below 2%. This ensures that isotope fractionation is computed incrementally in the presence of continuous fresh input, rather than over the full model time step. In addition, we derive an exact integration solution describing the isotopic evolution of the reservoir in an open system with simultaneous fresh ~~mixture~~input and ~~removed~~ product ~~simultaneously~~removal (Text S3). ~~Our goal is to~~By comparing the iterative method against this exact benchmark, we determine the optimal sub-~~timesteps that effectively reduce the impact of time step and minimize discrepancies in the simulated evolution of isotope composition of the reservoir between the Rayleigh equation and the integration method. Further details of the comparison~~step size that minimizes the discrepancy between the Rayleigh-based calculation and the open-system solution; further sensitivity tests are presented in Section 3.1.

3 Results

Building upon the isotope-enabled modeling framework established in Section 2, we evaluate the model's performance. The evaluation proceeds in two stages. First, we validate the iterative time-splitting method incorporated into the isotopic chemistry calculation (Section 3.1), demonstrating that our approach adequately resolves the isotope evolution in open systems with simultaneous mixing and reaction. Second, we assess the model's ability to

capture observed sulfur isotope signatures, focusing on the sulfur isotope effect ($\Delta\delta^{34}S\_SO_4^{2-}/SO_2$) and the site- and season-dependent $\delta^{34}S\_SO_4^{2-}$ across eastern China (Section 3.2).

3.1 Improving isotopic chemistry simulation and sensitivity tests

In previous studies, the initial isotopic composition of reactant ($\delta_{s,0}$) was calculated based on the isotopic composition of the product (δ_p) and the residual fraction of reactants f_{rem} using the Rayleigh equation (eq. 9-10), assuming no addition or mixing. This resulted in isotopic "reservoir effects" as the reaction progressed. The isotopic fractionation factor α>determines the direction of fractionation: when α > 1/α<1 preferentially enriches/depletes, heavy isotopes are preferentially enriched in the product and depletes/enriches heavy isotopes depleted in the residual reservoir. Investigating the; conversely, when α < 1, heavy isotopes are preferentially depleted in the product and enriched in the residual reservoir.

To illustrate the magnitude of the reservoir effect under realistic atmospheric oxidation of SO_2 via variousconditions, we consider the competing S(IV) oxidation pathways, including oxidation by: gas-phase OH radicals, aqueous-phase H_2O_2, O_3, and TMI-catalysis, and heterogeneous reaction. Using model results from Shao et al. (2019), who employed the GEOS-Chem model to quantify the contributions of these competing pathways to sulfate formation during a Beijing pollution episode, their respective contribution to sulfate formation wererereported contributions are 42.6%, 2.2%, 1.3%, 27.2%, and 26.7%, as derived from simulation results using GEOS-Chem model (Shao et al., 2019). Therespectively. Based on these pathway contributions, the calculated overall/net sulfur fractionation factor $\alpha^{34}S_{S(IV)}$ is 1.0063 at 0 °C. Therefore, the sulfate product favors the heavier isotopologues $^{34}SO_4^{2-}$ over $^{32}SO_4^{2-}$, leading to an increase in $\delta^{34}S\_SO_4^{2-}$ as the reaction progresses. This relationship depends on the fractionation fraction and the reaction extent. As shown in Figure 3, settingwith the initial $\delta^{34}S$ of SO_2 atset to 0‰, when f_{rem} becomesdrops to 70% and 20%, the $\delta^{34}S$ of the remainingresidual SO_2 rapidly drops to reaches approximately -2.2‰ and -10‰. Simultaneously,‰, while the $\delta^{34}S$ of the accumulated sulfate product reaches close toapproximately 5.2‰ and 2.5‰, respectively. This implies that the sulfur isotope difference between SO_2 and sulfate (The resulting $\Delta\delta^{34}S\_SO_4^{2-}/SO_2$) is 7.4‰ and 12.5‰, respectively. Due to ‰. As the reservoir effect, tremendously large approaches depletion (f_{rem}≈0), the apparent isotope fractionations will always be produced if the reservoir is close to being depleted (f_{rem}≈0). This phenomenon fractionation becomes unrealistically large. This challenges the applicabilitydirect application of the Rayleigh equation applied to scenarios involving simultaneousto systems where mixing and reaction occur simultaneously.

设置了格式

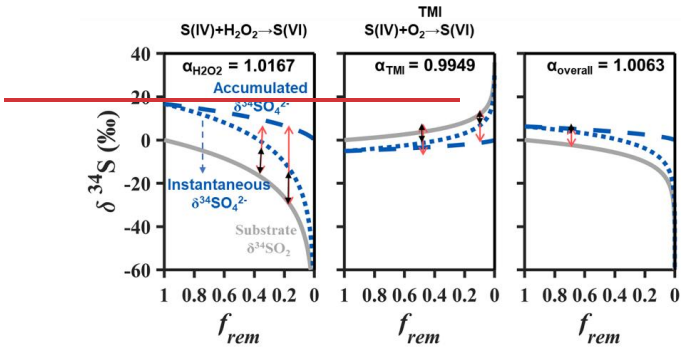

~~**Figure 3.** $\delta^{34}S$ values of residual reactant, instantaneous product, and the average isotopic composition of accumulated produce plotted as a function of a faction of remaining reactant in the closed system based on a Rayleigh equation. Investigating the sulfur isotopic fractionation during (a) aqueous-phase TMI-catalysis, (b) aqueous-phase H_2O_2 oxidation and (c) various competing S(IV) oxidation pathways, including oxidation by gas-phase OH radicals, aqueous-phase oxidation involving H_2O_2, O_3, TMI-catalysis, and heterogeneous reaction, their respective contribution to sulfate formation were 42.6%, 2.2%, 1.3%, 27.2%, and 26.7%, as derived from simulation results using GEOS-Chem model (Shao et al., 2019). The initial isotopic composition $\delta^{34}S$ values of the reactant is set to be 0‰. The fractionation factor for $^{34}S/^{32}S$ during aqueous oxidation by (a) H_2O_2, (b) TMI-catalyzed and (c) the overall competing S(IV) oxidation pathways are 1.0167, 0.9949, and 1.0063 at 0°C, respectively. The solid black line represents the variation of $\delta^{34}S$ values of residual reactant, and the blue dotted line and dashed line represent the variation of $\delta^{34}S$ values of instantaneous product and accumulated product, respectively.~~

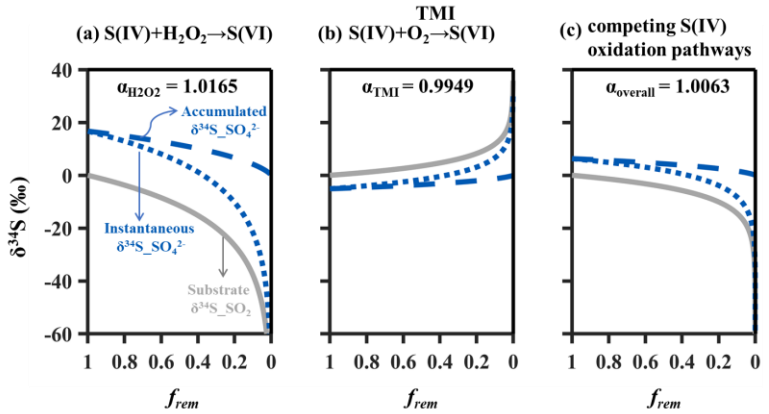

~~Based on~~

Figure 3. Rayleigh plot for sulfur isotope fractionations during SO_2 oxidation in a closed system with no external input and irreversible product removal. $\delta^{34}S$ values of the residual reactant (solid black line), instantaneous product (blue dotted line), and accumulated product (blue dashed line) are shown as a function of the fraction of remaining reactant based on a Rayleigh equation, with the initial $\delta^{34}S$ of SO_2 set to 0 ‰. Three scenarios are illustrated: (a) aqueous-phase H_2O_2 oxidation ($\alpha^{34}S$ = 1.0165 at 0 °C), (b) aqueous-phase TMI-catalyzed oxidation ($\alpha^{34}S$ = 0.9949 at 0 °C), and (c) the net isotope effect under competing S(IV) oxidation pathways ($\alpha^{34}S$ = 1.0063 at 0 °C). The pathway contributions in panel (c) competing S(IV) oxidation pathways—gas-phase OH oxidation (42.6%), aqueous H_2O_2 oxidation (2.2%), O_3 oxidation (1.3%), TMI-catalyzed oxidation (27.2%), and heterogeneous reactions (26.7%)—are derived from GEOS-Chem simulations (Shao et al., 2019).

Using the integration method ~~describing~~that describes the isotopic evolution of the reservoir in an open system ~~with simultaneous mixing and reaction (see (~~Text S3~~).),~~ Figure S1 illustrates that as the β value (the ratio of the instantaneous amount added to the removal) increases, the δ value of the reservoir progressively gets higher, with the external sources consistently contributing with a constant isotopic composition (δ_s) of 10‰. This emphasizes the importance of considering the mixing process when calculating the isotope effect. The overall apparent isotope fractionations are indeed the result of combined effects of the Rayleigh-like distillation process and the diffusion-driven isotope distributions (Guan and Liu, 2023). The combined processes with the mixing of fresh material and isotopic fractionation can lead to a smaller variation in ~~Δ^{34}S~~Δ$\delta^{34}S$_SO_4^{2-}/SO_2 than estimated by Rayleigh equation. ~~It indicated~~These results indicate that the optimal sub-timesteps ~~that~~ effectively reduce the ~~impact of~~ time-step impact and minimize discrepancies ~~in the simulated evolution of isotopic composition of the reservoir~~ between the Rayleigh-~~equation~~-based calculation and the integration method.

To mitigate the ~~significant~~numerical bias ~~in simulated isotopic composition introduced by~~that can arise when the Rayleigh equation ~~in the isotopic chemistry module~~is applied directly over a finite CTM time step, we implement an iterative time-splitting method. Firstly, the comparison between this iterative method and integration method in the open system helps determine the optimal sub-timesteps, effectively minimizing the biases in isotopic calculation when employing the Rayleigh equation. Figure S2 illustrates that the largest differences are observed for small reaction fraction and large fraction of fresh mixture relative to the initial substrate. A larger difference is expected when the differences between the isotopic composition of substrate and mixture increase and the isotope effect becomes stronger. For 50 sub-timesteps, good agreements are found in the calculated isotopic value of the reservoir between the iterative time-splitting method and the integrating method, assuming 0.3‰ is approximate to the average analytical precision of isotope. This indicates that the combination of the Rayleigh equation with the iterative method is capable of effectively simulating the progressive isotopic evolution of reservoirs with simultaneous mixing and isotopic fractionation.

We also conduct sensitivity tests to check the performance of the simulated isotopic composition of product with the optimized sub-timesteps. We choose 0.3‰ as the tolerance of this iterative time-splitting method. Figure S3 illustrates the deviation of δ-values for 1, 10, 50, and 100 sub-steps relative to the reference simulation with 1000 sub-steps. Notably, the largest

deviation occurs for a large fraction of reaction *f* and mixture, attributed to greater depletion in the reservoirs (α>1) and influence of mixing process. For 50 sub-steps, the maximum deviation is less than 0.1‰. This comparison confirms that the sub-timestep limiting reaction fraction *f* to approximately 2% is acceptable for reducing simulation bias, thus the value is adopted to improve the simulation.

The numerical comparison further shows that the largest differences between the direct Rayleigh calculation and the iterative method occur mainly over remote oceanic regions, where SO_2 emissions are low, reaction extents are high, and the SO_2 reservoir effect is strongest; in these regions, the iterative method reduces the simulated $\Delta\delta^{34}S\_SO_4^{2-}/SO_2$ by approximately 1.5‰–3.0‰ relative to the direct Rayleigh calculation applied over the full model time step. In regions with intensive anthropogenic activity, the influence is smaller but still non-negligible, with changes of approximately 0.3‰–1.0‰ in some polluted areas, demonstrating that the iterative time-splitting method improves the numerical accuracy of simulated sulfur isotope fractionation.

3.2 Model evaluation

3.2.1 ~~Reproduction~~Evaluation of sulfur isotope effect

As shown in Table 1, the sulfur isotopes exhibit distinctive fractionation during chemical reactions, including gas-phase, aqueous-phase, and heterogeneous reactions. It provides valuable information for investigating the relative importance of the different oxidation pathways converting SO_2 to sulfate. Gas-phase and aqueous-phase oxidation by H_2O_2 and O_3 produces sulfate that is enriched in ^{34}S (+15.1‰ to +19.9‰, depending on pH and temperature) relative to the initial SO_2 reservoir, while the SO_2 reservoir becomes depleted in ^{34}S. In contrast, TMI-catalyzed oxidation produces sulfate depleted in ^{34}S (–9.5 ± 3.1‰) relative to initial SO_2 (Harris et al., 2012a; Harris et al., 2012c; Harris et al., 2013; Harris et al., 2012b).

~~Figure~~Figures 4 and 5 ~~shows~~show the simulated spatial-temporal distribution of ~~daily~~near-surface $\delta^{34}S\_SO_2$ and $\delta^{34}S\_SO_4^{2-}$ ~~near ground level~~ for individual sulfur oxidation pathways through controlled experiments. We focus on the simulation results for the isotope effect resulting from individual sulfur oxidation pathways. The $\delta^{34}S$ of all emission sources is assumed to be 0‰. The model predicts a daily-mean range of $\delta^{34}S\_SO_4^{2-}$ ~~with~~of 8‰, 2‰~16‰, 0‰~6‰, and −8‰~0‰ via gas-phase oxidation by OH radical, and cloud-phase oxidation by H_2O_2, O_3, TMI-catalyzed O_2 over ~~Eastern~~eastern China, respectively. Correspondingly, a depleted ^{34}S in SO_2, and the daily-mean range of $\delta^{34}S\_SO_2$ = −5‰~1‰, −5‰~0‰, −3‰~−1‰, and 0.5‰~3‰, respectively. A ~~distinct~~relatively homogeneous spatial ~~distribution~~pattern of $\delta^{34}S\_SO_4^{2-}$ is observed~~, with homogeneity~~ for gas-phase oxidation (~8~~‰) and heterogeneous spatial distribution for~~‰), whereas aqueous-phase oxidations show more heterogeneous spatial distributions. The simulated spatial-temporal distribution of $\delta^{34}S\_SO_4^{2-}$ depends on the relative importance of different oxidation pathways and the ratio of mixed SO_2 to formed sulfate within ~~an infinitesimal~~each model time ~~interval Δt at each grid cell~~step. Unlike gas-phase reactions, cloud and aqueous phase chemistry highly depend on the geographical distribution of cloud coverage and liquid water content. ~~While the~~The spatial ~~temporal~~ distribution of simulated $\delta^{34}S\_SO_2$ is more sensitive to the mixing rate of SO_2~~, the Eastern~~; in

eastern China ~~region with high~~, where SO_2 emission intensity ~~effectively offsets~~is high, the reservoir effect~~, showing~~ is effectively offset, resulting in slight regional differences.

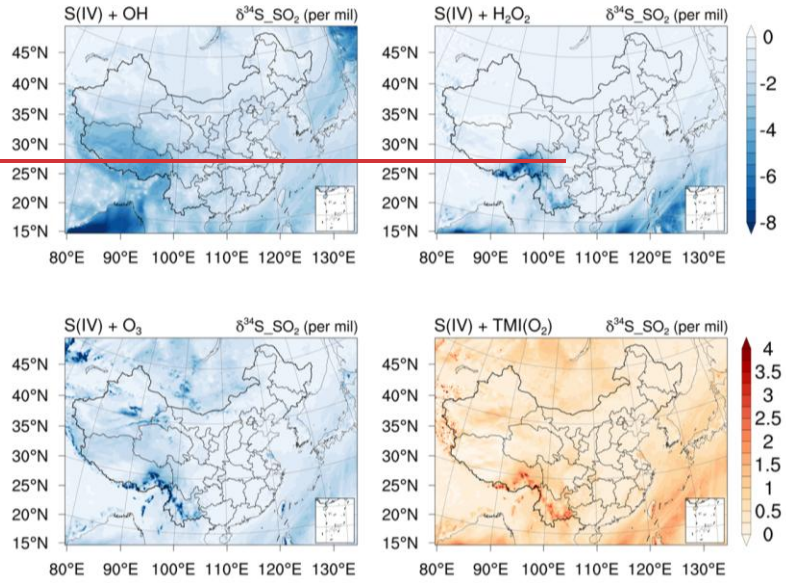

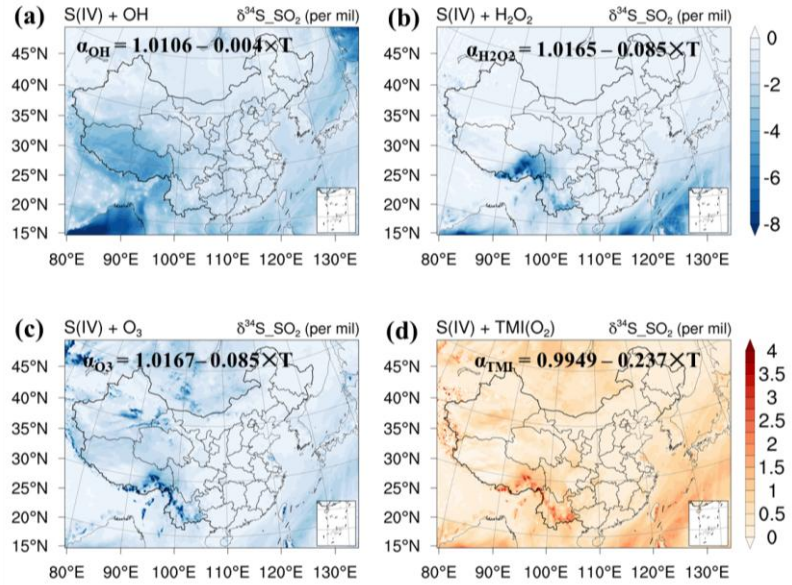

Figure 4. ~~The simulated~~Simulated spatial~~-temporal~~ distribution of ~~daily~~near-surface $\delta^{34}S\_SO_2$ ~~near~~

设置了格式: 字体: +西文正文 (Calibri), 字体颜色: 自动设置

设置了格式: 字体: +西文正文 (Calibri), 字体颜色: 自动设置

设置了格式: 字体: +西文正文 (Calibri), 字体颜色: 自动设置

设置了格式: 字体: +西文正文 (Calibri), 字体颜色: 自动设置

设置了格式: 字体: +西文正文 (Calibri), 10 磅, 字体颜色: 自动设置

设置了格式: 字体: +西文正文 (Calibri), 字体颜色: 自动设置

~~ground level~~ for individual sulfur oxidation pathways ~~through controlled experiments.~~ Each panel shows the result of a sensitivity experiment in which only one oxidation pathway is active: (a) gas-phase oxidation by OH radical, (b) cloud-phase oxidation by H_2O_2, (c) cloud-phase oxidation by O_3, and (d) cloud-phase oxidation by TMI-catalyzed O_2. ~~The simulation runs through~~All simulations are for December 2015. The sulfur isotopic composition of all emission sources is ~~assumed~~set to ~~be~~ 0~~‰. This approach minimizes~~‰ to minimize the impact of source fingerprint, ~~providing a better representation~~reflecting the direction and magnitude of the isotope ~~effect resulting from isotopic~~ fractionation ~~and dynamic mixing processes~~specific to each pathway. Positive values indicate ^{34}S enrichment in residual SO_2; negative values indicate depletion.

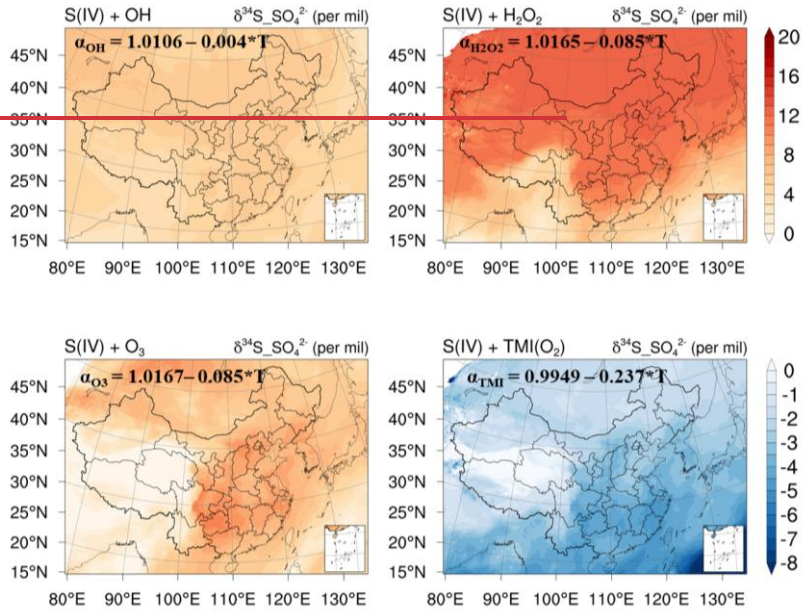

设置了格式: 字体: +西文正文 (Calibri), 字体颜色: 自动设置

设置了格式: 字体: +西文正文 (Calibri)

设置了格式: 字体: +西文正文 (Calibri)

设置了格式: 字体: +西文正文 (Calibri)

设置了格式: 字体: +西文正文 (Calibri)

设置了格式: 字体: +西文正文 (Calibri)

设置了格式: 字体: +西文正文 (Calibri)

设置了格式: 字体: +西文正文 (Calibri)

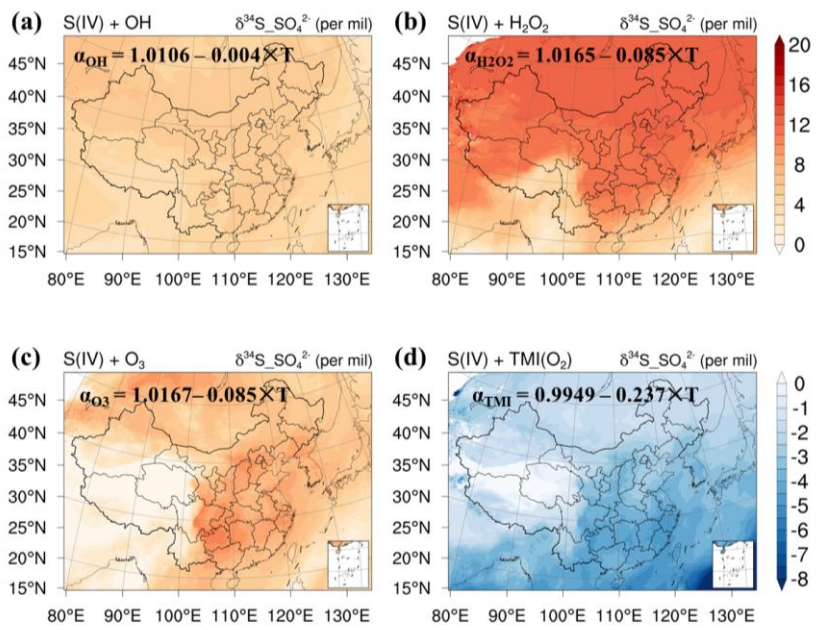

Figure 5. Same as Figure 4 ~~except,~~ but for ~~daily $\delta^{34}S\_SO_4^{2-}$~~ near ~~the ground level.~~

~~Although $\delta^{34}S\_SO_4^{2-}$ has been reported in previous studies, the large range and variation of $\delta^{34}S$ in sulfur-containing sources (coal, crude oil, biomass, etc.) hinder direct validation of the model with observations. To allow direct comparison and reduce uncertainties, we focus on $\delta^{34}S$ data in $PM_{2.5}$ and SO_2 collected simultaneously at the same site. While the available observed data is limited, only observational daily data from Nanjing city (118.5°E, 32.1°N) during the summer (July 6th to August 30th, 2014) and winter (January 1st to January 23rd, 2015) are chosen to validate the modeled sulfur isotope effects ($\Delta\delta^{34}S\_SO_4^{2-}/SO_2$) near the~~ surface ~~(below 1 km) (Chen et al., 2017). As shown in Figure 6(b), observed and simulated sulfur isotopic composition ($\delta^{34}S\_SO_2$, $\delta^{34}S\_SO_4^{2-}$) as well as $\Delta\delta^{34}S\_SO_4^{2-}/SO_2$ in Nanjing city are compared. The mean simulated and observed $\Delta\delta^{34}S\_SO_4^{2-}/SO_2$ are 5.50‰±1.66‰ and 3.27‰±0.76‰ in summer (n=25, R=0.76, NMB=54.8%), 6.54‰±1.91‰ and 3.39‰±1.68‰ in winter (n=16, R=0.70, NMB=35.3%), respectively. The isotope-enabled model can quantitatively reproduce the isotopic effect during SO_2-$\delta^{34}S\_SO_4^{2-}$. Panels show sensitivity experiments with~~ individual oxidation ~~processes, presenting enriched ^{34}S in sulfate and depleted ^{34}S in SO_2. Overall, the model also performs well with the seasonal variation of isotope effect and reflects the advantage of the real-time feedback between mixing and reservoir effect due to the isotopic fractionation. The model provides a reliable framework of atmospheric sulfur chemistry for simulating its isotopic composition.~~

设置了格式: 字体: +西文正文 (Calibri), 字体颜色: 自动设置

设置了格式: 字体: +西文正文 (Calibri), 字体颜色: 自动设置

设置了格式: 字体: +西文正文 (Calibri), 字体颜色: 自动设置, 图案: 清除

设置了格式

设置了格式

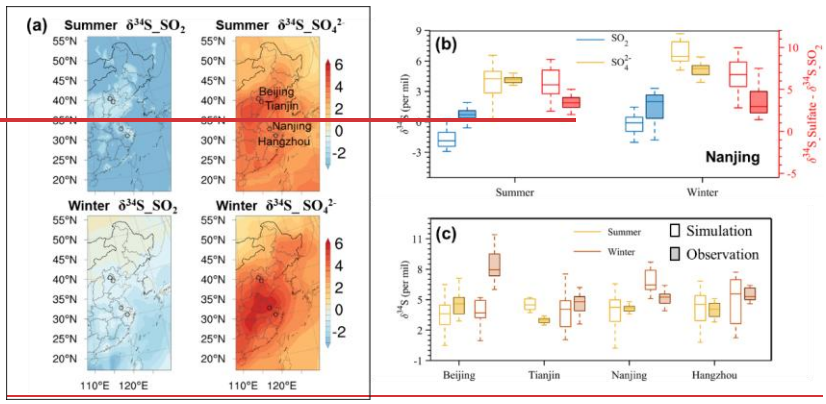

~~Figure 6. (a)~~ ~~The seasonal and spatial simulation of sulfur isotopic composition ($\delta^{34}S\_SO_2$, $\delta^{34}S\_SO_4^{2-}$) over Eastern China during summer (June to August) and winter (December to February). **(b)** The model validation by comparing observed and simulated sulfur isotopic composition ($\delta^{34}S\_SO_2$, $\delta^{34}S\_SO_4^{2-}$) as well as the sulfur isotope effect in Nanjing city during the summer and winter of 2014. **(c)** The comparison between seasonal variations in observed and simulated $\delta^{34}S\_SO_4^{2-}$ in $PM_{2.5}$ across Eastern China's cities.~~

~~The simulated results are comparable with the observations, although the model underestimates $\delta^{34}S\_SO_2$ due to the overestimation of $\Delta\delta^{34}S\_SO_4^{2-}/SO_2$. The model's overestimation of $\Delta\delta^{34}S\_SO_4^{2-}/SO_2$ during both summer and winter seasons could be attributed to the underestimation of aqueous~~pathways active: (a) gas-phase ~~TMI-catalyzed oxidation pathway, the only pathway recently found to deplete ^{34}S in sulfate relative to SO_2, resulting from isotopic fractionation $\alpha<1$. Sulfur oxidation by TMI-catalyzed O_2 and NO_2, both involving electron transfer reaction between S(IV) and catalyst or oxidant to initiate radical chain oxidation mechanisms, would exhibit similar isotopic fractionation. Previous studies have indicated that the~~ OH, (b) aqueous-phase ~~TMI-catalyzed oxidation pathway is underestimated in the current atmospheric chemical transport models, contributing 9%~18% to sulfate production globally (Alexander et al., 2009; Itahashi et al., 2022). The heterogeneous reactions via TMI-catalyzed oxidation on deliquesced aerosol particles can contribute 14%~92% to sulfate production during the heavy pollution period in Northern China (Shao et al., 2019; Wang et al., 2021). Currently, laboratory studies also show that enhanced multiphase oxidation of SO_2 by NO_2 in deliquesced aerosol particles (Wang et al., 2016; Liu and Abbatt, 2021), and the relative importance of NO_2 oxidation was also estimated by WRF-chem model coupled with the aerosol water chemistry module (Tao et al., 2020). The accurate investigation of isotopic fractionation factors for the NO_2 oxidation pathway is currently lacking. It is important to note that our developed isotope-enabled model does not currently incorporate the multiphase chemistry of SO_2 in aerosol liquid water. Instead, we employ the obtained sulfur isotope fractionation during heterogeneous oxidation of SO_2 on mineral dust ($\alpha > 1$) (Harris et al., 2012b) to represent the overall isotope effect of all heterogeneous reactions at the interface of deliquesced aerosol particles. This also introduces some biases into the simulated results. Therefore, additional laboratory research is needed to determine these specific isotopic fractionations during heterogeneous/multiphase chemistry~~ H_2O_2, (c) aqueous-phase O_3, and (d) TMI-catalyzed O_2 oxidation, all for December 2015 with $\delta^{34}S\_SO_2$ emission = 0 ‰. Positive values indicate ^{34}S enrichment in sulfate; negative values indicate depletion.

带格式的: 正文, 居中, 缩进: 首行缩进: 0.25 厘米, 无孤行控制

设置了格式: 字体: 12 磅

设置了格式: 字体: 12 磅

域代码已更改

设置了格式: 字体: +西文正文 (Calibri)

设置了格式: 字体: 12 磅, 字体颜色: 文字 1

设置了格式: 字体颜色: 黑色

~~3.2.2 Significant spatial-temporal variation of $\delta^{34}SO_4^{2-}$~~

~~Our isotope-enabled model performs relatively well for the sulfur isotope effect. Therefore, we are confident in comparing~~We evaluate the oxidation isotope module using the sulfur isotope effect $\Delta\delta^{34}S\_SO_4^{2-}/SO_2$, the isotopic difference between sulfate and SO_2. Because $\Delta\delta^{34}S\_SO_4^{2-}/SO_2$ depends on the relative isotope fractionation among oxidation pathways rather than on the absolute $\delta^{34}S$ of emitted SO_2, it is less sensitive to source isotopic assumptions and provides a more direct evaluation of the oxidation module.

Simultaneous $\delta^{34}S$ observations of $PM_{2.5}$ sulfate and SO_2 are available at Nanjing (118.5°E, 32.1°N) for summer (6 July to 30 August 2014) and winter (1–23 January 2015) (Chen et al., 2017). As shown in Figure 6(b), the simulated $\Delta\delta^{34}S\_SO_4^{2-}/SO_2$ averaged 5.50‰ ± 1.66‰ (summer) and 6.54‰ ± 1.91‰ (winter), compared with the observed means of 3.27‰ ± 0.76‰ (summer, n = 25, R = 0.76, NMB = 54.8%) and 3.39‰ ± 1.68‰ (winter, n = 16, R = 0.70, NMB = 35.3%), respectively. The overall simulated $\Delta\delta^{34}S\_SO_4^{2-}/SO_2$ is 6.11 ± 1.85‰, compared to the observed mean of 3.43 ± 1.11‰. The model captures the enrichment direction and seasonal variation but systematically overestimates the magnitude. This overestimation is physically consistent with the underrepresented ^{34}S-depleting TMI-catalyzed oxidation pathway and the absence of aerosol water multiphase chemistry in the current mechanism. Further discussion is in Section 4.1.

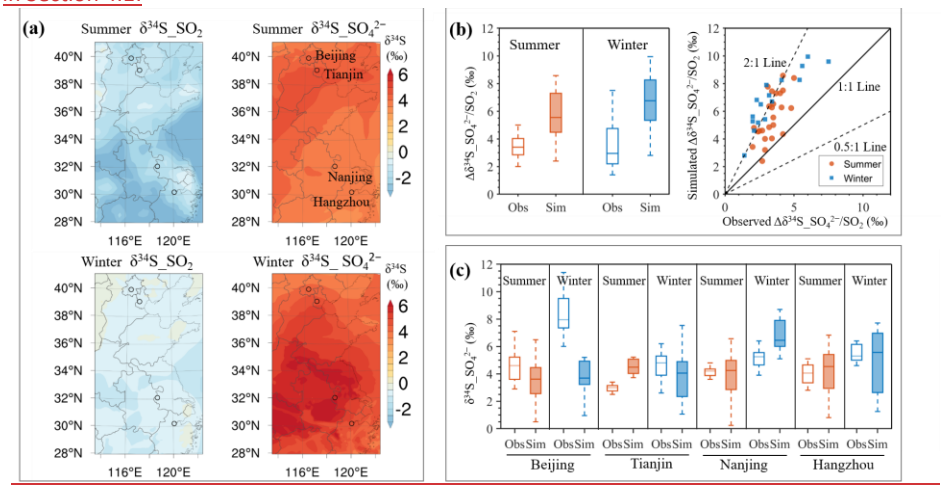

Figure 6. Comparison between simulated and observed sulfur isotope composition over eastern China. (a) Simulated seasonal mean spatial distributions of sulfur isotopic composition ($\delta^{34}S\_SO_2$, $\delta^{34}S\_SO_4^{2-}$) over eastern China for summer (June–August) and winter (December–February) of 2015. (b) Comparison of simulated and observed $\delta^{34}S\_SO_2$, $\delta^{34}S\_SO_4^{2-}$, and $\Delta\delta^{34}S\_SO_4^{2-}/SO_2$ at Nanjing during the summer and winter 2014. $\Delta\delta^{34}S\_SO_4^{2-}/SO_2$ primarily reflects oxidation-induced isotope fractionation and is less sensitive to the assumed $\delta^{34}S$ of emission sources, providing a more direct evaluation of the oxidation isotope module. (c) Seasonal comparison of simulated and observed $\delta^{34}S\_SO_4^{2-}$ in $PM_{2.5}$ across multiple cities in

eastern China, simulated values correspond to the same seasonal periods as the observations at each site. In panels (b) and (c), "Obs" denotes observation and "Sim" denotes simulation.

3.2.2 Site- and season-dependent $\delta^{34}S\_SO_4^{2-}$

The $\Delta\delta^{34}S\_SO_4^{2-}/SO_2$ evaluation at Nanjing (Section 3.2.1) shows that the oxidation module captures the direction and seasonal variability of the isotope effect, albeit with a systematic overestimation. We next compare the simulated ~~and observed~~absolute $\delta^{34}S\_SO_4^{2-}$ with observations, noting that absolute $\delta^{34}S\_SO_4^{2-}$ ~~in $PM_{2.5}$,~~is influenced by both oxidation fractionation and the assumed $\delta^{34}S$ of emitted SO_2. Figure 6(c) presents the model's comparison with a compilation of $\delta^{34}S\_SO_4^{2-}$ observations across ~~Eastern~~eastern China, including Beijing (Han et al., 2016b; Han et al., 2017; Wei et al., ~~2018a; Han et al., 2016b~~2018), Tianjin (Han et al., 2022; Ding et al., 2022), Nanjing ~~(Chen et al., 2017)~~(Chen et al., 2017), and Hangzhou city (Lin et al., 2022).

The simulated daily mean $\delta^{34}S\_SO_4^{2-}$ in Nanjing and Hangzhou ~~don't~~do not significantly differ from the observed values. Specifically, for Nanjing, the simulated and observed $\delta^{34}S\_SO_4^{2-}$ were 3.88‰±1.63‰ and 4.01‰±0.39‰ in summer (n=25, R= 0.74, NMB= −4.4%), and 6.47‰±1.09‰ and 4.80‰±0.84‰ in winter (n=16, R= 0.76, NMB= 34.8%), respectively. For Hangzhou, the simulated and observed $\delta^{34}S\_SO_4^{2-}$ were 3.91‰±1.77‰ and 3.50‰±1.25‰ in summer (n=8, R= 0.88, NMB= 10.4%), and 4.63‰±2.37‰ and 4.95‰±0.62‰ in winter (n=8, R= 0.84, NMB= −10.5%), respectively. Regarding Tianjin, the simulated and observed $\delta^{34}S\_SO_4^{2-}$ were 3.88‰±1.73‰ and 4.20‰±1.26‰ in winter (n=34, R= 0.83, NMB= −11.0%), the model (4.40‰±1.62‰) slightly overestimates observed $\delta^{34}S\_SO_4^{2-}$ (2.75‰±0.45‰) in summer (n=12, R= 0.87, NMB= 57.4%). This difference remains within the acceptable 2‰ range for the sulfur isotope effect, considering a ±10% uncertainty in the relative significance of enriched or depleted sulfur oxidation pathways. However, the model (3.99‰±1.86‰) underestimates the observed $\delta^{34}S\_SO_4^{2-}$ (7.94‰±1.41‰) about 50% in Beijing winter (n=16, R= 0.79, NMB= −50.5%). ~~Overall, the model fails to capture the observed seasonal pattern with winter maximum and summer minimum for $\delta^{34}S\_SO_4^{2-}$ in northern China.~~

4 Discussion

The model evaluation in Section 3 demonstrates that the isotope-enabled framework captures the enrichment direction and seasonal variability of the sulfur isotope effect. However, site- and season-dependent biases remain, including the systematic overestimation of $\Delta\delta^{34}S\_SO_4^{2-}/SO_2$ and the wintertime underestimation of $\delta^{34}S\_SO_4^{2-}$ at Beijing. Section 4.1 discusses the sources of the biases. Section 4.2 extends the discussion to broader implications inferred by combining model results with literature evidence. It examines how isotopic fractionation during combustion and flue gas desulfurization (FGD) processes may reconcile the apparent offset between fuel $\delta^{34}S$ values and observed aerosol $\delta^{34}S$, and discusses what this implies for source apportionment studies.

4.1 Model-demonstrated results: oxidation-driven versus source-driven biases

The overestimation of $\Delta\delta^{34}S\_SO_4^{2-}/SO_2$ at Nanjing (NMB = 35–55%) is attributed to the insufficient representation of the TMI-catalyzed oxidation pathway — the only known oxidation

pathway that produces sulfate depleted in ^{34}S relative to SO_2 ($\alpha = 0.9949$, $\varepsilon \approx -5.1‰$). Previous studies have indicated that the aqueous-phase TMI-catalyzed oxidation pathway is underestimated in the current atmospheric chemical transport models, contributing 9%~18% to sulfate production globally (Alexander et al., 2009; Itahashi et al., 2022), while heterogeneous reactions via TMI-catalyzed oxidation on deliquesced aerosol particles can contribute 14%–92% to sulfate production during the heavy pollution period in Northern China (Shao et al., 2019; Wang et al., 2021). Furthermore, model parameterizations of Fe and Mn concentrations are biased low in East Asia (Itahashi et al., 2022), which directly suppresses the simulated TMI-catalyzed sulfate production. Our model does not currently include TMI-catalyzed oxidation in aerosol liquid water. Instead, we employ the obtained sulfur isotope fractionation during heterogeneous oxidation of SO_2 on mineral dust ($\alpha_s > 1$) (Harris et al., 2012b) to represent the overall isotope effect of all heterogeneous reactions at the interface of deliquesced aerosol particles~~This discrepancy may indicate the presence of emission sources with enriched $\delta^{34}SO_2$ during winter. As shown in Figure 1 and Table S1, the $\delta^{34}S$ values for coal samples collected in northern China regions, including Beijing city, Hebei and Henan provinces, were 7.4±16.1‰, 3.5±6.6‰ and 6.4±1.0‰, respectively. The increased residential heating in northern China aggravates pollution conditions, contributing about 46% of the monthly averaged $PM_{2.5}$ concentration (Zhang et al., 2017). Consequently, the distinct seasonal shift in energy type (coal, biomass, clean energy, etc.) and activity (cooking, heating, etc.) can substantially influence the $\delta^{34}S\_SO_4^{2-}$ signature in aerosol samples (Wei et al., 2018b). The wide range of $\delta^{34}S$ values of sulfur-containing fuels, combined seasonal shift in energy usage, complicates direct comparisons between modeled and observed $\delta^{34}S\_SO_4^{2-}$. Further details on the influences of isotope fractionation during combustion processes on the large uncertainties in modeled $\delta^{34}S\_SO_4^{2-}$ are discussed in Section 4.~~

~~**4 Discussion**~~

, which likely introduces additional biases. Currently, laboratory studies also show enhanced multiphase oxidation of SO_2 by NO_2 in deliquesced aerosol particles (Wang et al., 2016; Liu and Abbatt, 2021), but isotopic fractionation factors for this pathway are currently lacking and require further measurement.

The site- and season-dependent $\delta^{34}S\_SO_4^{2-}$ biases can be grouped into two categories: Category 1 — Oxidation-driven biases. At Nanjing, Hangzhou, and Tianjin winter, the $\delta^{34}S\_SO_4^{2-}$ biases are broadly consistent in direction with the known overestimation of $\Delta\delta^{34}S\_SO_4^{2-}/SO_2$ by the oxidation module. This confirms that the $\delta^{34}S\_SO_2 = 0‰$ assumption is a reasonable approximation for the well-mixed regional SO_2 emissions at these locations. The remaining bias is therefore predominantly oxidation-driven, reflecting the underrepresented TMI-catalyzed pathway and simplified heterogeneous chemistry noted above.

Category 2 — Source-driven biases. By contrast, at Beijing winter, the model (3.99‰ ± 1.86‰) underestimates observed $\delta^{34}S\_SO_4^{2-}$ (7.94‰ ± 1.41‰) by ~50% (NMB = −50.5%). This contrasts with the oxidation module's upward bias in $\Delta\delta^{34}S$, which would drive $\delta^{34}S\_SO_4^{2-}$ above observation. This reversed bias direction provides a clear diagnostic that the dominant error originates from the source assumption rather than from the oxidation module.

域代码已更改

设置了格式: 字体: +西文正文 (Calibri)

As shown in Figure 1 and Table S1, documented coal $\delta^{34}S$ in northern China — including Beijing, Hebei, and Henan — are substantially higher than 0‰, with means of 7.4 ± 16.1‰, 3.5 ± 6.6‰, and 6.4 ± 1.0‰, respectively. Enhanced residential heating in northern China contributes about 46% of the monthly averaged $PM_{2.5}$ concentration (Zhang et al., 2017), providing a localized source of SO_2 with elevated $\delta^{34}S$. If Beijing winter SO_2 carries $\delta^{34}S \approx 7‰$ (the mean coal value) instead of 0‰, the modeled $\delta^{34}S\_SO_4^{2-}$ would increase from ~4.0‰ to ~6–7‰ after accounting for oxidation-driven enrichment, approaching the observed 7.94‰. Consequently, the distinct seasonal shift in energy type (coal, biomass, clean energy, etc.) and activity (cooking, heating, etc.) can substantially affect aerosol $\delta^{34}S\_SO_4^{2-}$ (Wei et al., 2018), complicating direct model–observation comparisons where strong localized combustion sources are present.

4.2 Interpretive implications: combining model results with literature evidence

The preceding discussion reflects what is directly resolved by the isotope-enabled model. We now extend the discussion to broader implications inferred by combining our model results with literature evidence on emission-source isotopic signatures, combustion fractionation, and FGD.

Assuming a fixed $\delta^{34}S\_SO_2$ of 0‰ for all anthropogenic emissions of SO_2, ~~Figure 6 demonstrates~~ the model's ~~capability~~ability to reproduce observed $\delta^{34}S\_SO_2$ ~~and $\delta^{34}S\_SO_4^{2-}$. This good agreement reveals $\delta^{34}S\_SO_2$ for~~ SO_4^{2-} (Section 3.2.2) suggests that well-mixed anthropogenic SO_2 emissions ~~is expected~~are characterized by $\delta^{34}S$ values close to ~~be approximately~~ 0‰. However, compiled ~~data on the~~ anthropogenic $\delta^{34}S$ values of SO_2 emission sources in ~~Eastern~~eastern China, including coal, crude oil, and biomass, range from 1‰ to 10‰ (Hong et al., 1993; Guo et al., 2016; Chen et al., 2017). This discrepancy ~~sparked our curiosity and motivated further investigation~~points to a systematic ^{34}S depletion process in emitted SO_2.

~~As shown in Figure 7, both residential and industrial combustion experiments revealed that the sulfate in ash particles enriched ^{34}S, while emitted SO_2 depleted in ^{34}S (−10‰ ~ −5‰) relative to the sulfur-containing fuels (Hong et al., 1993; Chen et al., 2017). Flue gas desulfurization also introduces isotopic fractionation, with the outlet emitted SO_2 showing a depletion in ^{34}S relative to the inlet SO_2 (calculate~~As shown in Figure 7, residential and industrial combustion experiments show that the sulfate in ash particles enriched ^{34}S, while emitted SO_2 is depleted in ^{34}S (−10‰ ~ −5‰) relative to the fuel (Hong et al., 1993; Chen et al., 2017). FGD further introduces isotopic fractionation, with the outlet SO_2 isotopically lighter than the inlet SO_2 (calculated apparent sulfur isotope enrichment factors ε*= −5.5‰) (Derda et al., 2007). ~~This likely contributes to~~These documented combustion and FGD fractionation patterns are temporally consistent with the abrupt ~~change~~decline in ~~the lighter~~ $\delta^{34}S\_SO_4^{2-}$ ~~observed over~~with continuous long-term aerosol observation (shifting from 5‰ ~ 10‰ before 1999 to 0‰ ~ 5‰ at Tsuruoka, Japan) (Oduro et al., 2012) and wet precipitation records (~~dropping~~ from 6.6‰ in 2010 to −0.1‰ in 2017 at Jiaozuo city, China) (Zheng et al., 2024). This ~~phenomenon coincidentally corresponds to~~observed $\delta^{34}S$ decline coincides with the widespread adoption of ~~flue gas desulfurization~~FGD technology in coal-fired industries after 2000 ~~(Liu, 2019).~~(Liu, 2019), although other concurrent factors — such as changes in the relative contribution of coal, oil, and biomass combustion sources, shifts in the geographic distribution of SO_2 emissions, and

variations in atmospheric oxidation pathways — may also contribute to the observed trends. Establishing a direct causal linkage between FGD deployment and the recorded $\delta^{34}S$ decline would require a dedicated study combining long-term field observations with systematic source sampling and experimental study of isotopic fractionation during combustion and FGD processes, which is beyond the scope of the present analysis. This temporal coherence, nevertheless, suggests that FGD-induced isotopic fractionation is a plausible contributing factor worth further investigation.

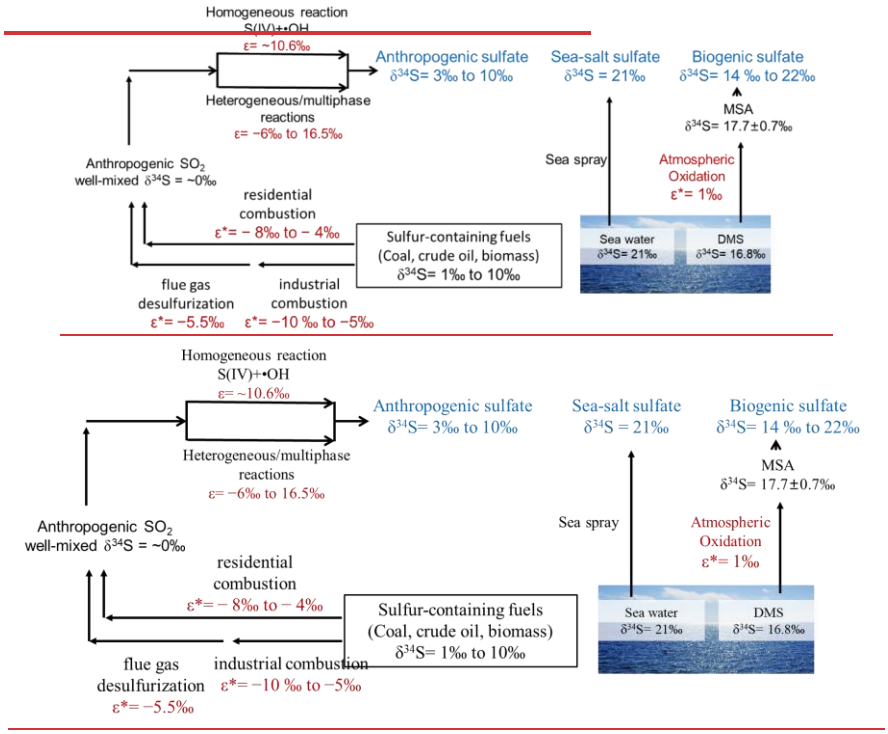

Figure 7. Schematic diagram of different processes and associated isotope enrichment factors for transformations of major sulfur-containing species to biogenic, anthropogenic, and sea-salt sulfate in the atmosphere. The sulfur isotopic compositions ($\delta^{34}S$) of anthropogenic sources (coal, crude oil, and biomass, etc.) in ~~Eastern~~eastern China are compiled from Hong et al.(1993), Guo et al. (2016) and Chen et al. ~~(2017)~~(2017). The $\delta^{34}S$ of sea-salt sulfate, DMS, MSA, biogenic sulfate, and the apparent enrichment factor during atmospheric oxidation of DMS to MSA are referenced from Oduro et al. (2012). The isotope enrichment factor (ε) for oxidation pathways of sulfur are listed in Table 1. Apparent enrichment factors (ε*) during residential combustion are investigated by Hong et al. (1993) and Chen et al. ~~(2017).~~(2017). ε* during industrial combustion and ~~flue gas desulfurization~~FGD are reported by Hong et al. (1993) and Derda et al.

(2007), respectively. Because the combustion experiments are not comparable to the carefully controlled environment of laboratory studies, ~~it can't obtain the~~these experiments cannot yield accurate sulfur isotopic fractionation factors, thus, we employ the sulfur isotope difference between initial $\delta^{34}S$ of sulfur-containing fuels and $\delta^{34}S$ of outlet-emitted SO_2 to interpret ε^* during combustion and ~~flue gas desulfurization~~FGD processes.

~~Additionally, the sulfur oxidation pathway produces enriched sulfate with $\Delta\delta^{34}S\_SO_4^{2-}/SO_2$ at 6‰ ~ 8‰. Thus, the isotopic fractionation during combustion/flue gas desulfurization and chemical processes somewhat offsets each other, leading to only a slight difference of $\delta^{34}S$ between sulfur-containing fuels and airborne sulfate aerosol ($\delta^{34}S$ = 1‰ ~ 8‰). This emphasizes a complex isotope effect of sulfur chemistry during combustion and gas desulfurization. Failure to distinguish between $\delta^{34}S$_fuels and their emitted $\delta^{34}S\_SO_2$ (characteristically depleted in ^{34}S) may lead to significant discrepancies in source apportionment using the isotopic tracing method.~~

Additionally, the sulfur oxidation pathway produces enriched sulfate with $\Delta\delta^{34}S\_SO_4^{2-}/SO_2$ at 6‰ ~ 8‰. The emission-side ^{34}S depletion and the oxidation-side ^{34}S enrichment thus partly counterbalance each other, leading to only a modest net difference between fuel $\delta^{34}S$ and airborne sulfate $\delta^{34}S$ (typically 1–8‰) (Figure 7). This emphasizes a complex isotope effect of sulfur chemistry during combustion and FGD. Using fuel $\delta^{34}S$ directly as the SO_2 source end-member — without correcting for the ^{34}S depletion introduced by combustion and FGD — artificially elevates the source signature, causing systematic underestimation of the contribution of sulfur-containing fuels with significant combustion fractionation and overestimation of sources with $\delta^{34}S$ near 0‰. An independent study by Feng et al. (2023) quantified this effect: using high-time-resolution $\delta^{34}S$ observations during haze episodes in Northern China, they found that neglecting coal-combustion ^{34}S fractionation caused the coal contribution to be underestimated by 17%–38% of secondary sulfate. These quantitative findings corroborate the deductive evidence from our model and underscore the necessity of incorporating both emission-side and oxidation-side isotopic fractionation into the end-member framework for reliable source apportionment.

5 Conclusions and future atmospheric implications

~~Understanding how isotopes~~Isotopic fingerprints of atmospheric chemicals ~~behave is crucial for identifying~~provide essential constraints on their sources and ~~the~~ chemical ~~processes they undergo. We~~pathways. Here, we developed an isotope-enabled ~~chemical transport model~~ CTM to overcome the limitations of conventional mixing models~~, simulating~~. The model tracks four sulfur isotopologues ~~($^{32}SO_2$, $^{34}SO_2$, $^{32}SO_4^{2-}$, $^{34}SO_4^{2-}$) with~~ ($^{32}SO_2$, $^{34}SO_2$, $^{32}SO_4^{2-}$, $^{34}SO_4^{2-}$) and uses an iterative time-splitting method to ~~minimize~~reduce the Rayleigh-equation bias~~. The framework successfully quantifies~~ in open atmosphere. It reproduces pathway-specific fractionation: gas-phase (OH) and aqueous-phase (~~H_2O_2/O_3~~)H_2O_2/O_3) oxidation enriches sulfate in ~~^{34}S~~^{34}S (+15.1‰ to +19.9‰), while TMI-catalyzed reactions deplete ~~^{34}S~~^{34}S (–9.5 ± 3.1‰). ~~Critically, it reproduces the observed mean~~ The model captures sulfate ^{34}S enrichment and the spatial and seasonal patterns of the sulfur isotope effect ~~(~~across eastern China (simulated

$\Delta\delta^{34}S\_SO_4^{2-}$ ~~/SO_2^-~~/SO_2 = 6.11±1.85‰; observed = 3.43±1.11~~‰) across Eastern China and reveals distinct spatiotemporal patterns—winter maxima in northern cities (Beijing: 7.94 ± 1.41‰) linked to high-$\delta^{34}S$ coal combustion, contrasting with summer minima driven by aqueous oxidation dominance. However, it is worth noting that~~ ‰).

The remaining site- and season-dependent biases can be separated into two diagnostic categories. The systematic overestimation of ~~$\Delta\delta^{34}S$ may be due to~~ $\delta^{34}S\_SO_4^{2-}$ is primarily attributable to the underrepresented contribution of the ^{34}S-depleting TMI~~-catalysis and~~-catalyzed pathway, simplified heterogeneous chemistry (using mineral dust α >1~~). Previous studies have shown~~), and the absence of aerosol water multiphase chemistry — well-recognized limitations common to current-generation CTMs. By contrast, the wintertime underestimation of $\delta^{34}S\_SO_4^{2-}$ at Beijing represents a source-driven bias. Because the trend reverses the direction expected from oxidation-induced fractionation, this indicates that the $\delta^{34}S\_SO_2$ = 0‰ assumption—rather than the oxidation module—is the dominant source of error in regions where strong localized combustion sources have elevated $\delta^{34}S$. This bias attribution allows the model to distinguish oxidation-driven from source-driven biases and to constrain oxidation-pathway contributions.

Taken together with the documented higher $\delta^{34}S$ values of coal (1‰–10‰), the model's ability to reproduce observed $\delta^{34}S\_SO_4^{2-}$ under the $\delta^{34}S\_SO_2$ = 0‰ emission assumption implies that ~~SO_2 emissions were depleted in ^{34}S (~10‰ to ~5‰) relative to fuels ($\delta^{34}S$ = 1‰~10‰) due to isotopic fractionation~~combustion- and FGD-related ^{34}S depletion in emitted SO_2 (ε* ≈ −5.5‰; Derda et al., 2007) is largely counterbalanced by the ^{34}S enrichment during ~~combustion/flue gas desulfurization (ε* ≈ −5.5‰). The good agreement of $\delta^{34}S$ between simulation and observation helps us~~atmospheric SO_2 oxidation ($\Delta\delta^{34}S$ ≈ +6 to ~~make a fundamental finding~~ +8‰). This counterbalancing explains why ambient sulfate $\delta^{34}S$ is often close to that ~~this isotopic depletion counterbalances oxidation enrichment ($\Delta\delta^{34}S$ = +6 ~ +8‰) during the $SO_2 \rightarrow SO_4^{2-}$ reactions, explaining an approximate value between $\delta^{34}S$ of~~ of sulfur-containing fuels~~ and ambient samples. Ignoring this effect may cause~~. Neglecting the emission-side fractionation therefore introduces systematic bias into isotope-based source apportionment~~ errors~~, underestimating the contribution of fuels with significant combustion fractionation while overestimating sources with $\delta^{34}S$ near 0‰. Our study highlights that incorporating both emission-side and oxidation-side fractionation into source apportionment frameworks is therefore essential for reliable results.

Our study also ~~guides~~informs future sampling~~,~~ by proposing simultaneous measurement of the isotopic composition of gaseous precursors and aerosols~~. This approach aims to enhance better~~, which would improve the interpretation of isotopic effects during chemical processes and ~~achieve~~enable more accurate source identification. ~~In addition~~Nevertheless, conducting direct comparisons between simulations and field observations remains challenging, primarily due to the limited availability and large uncertainties ~~in~~of the isotopic composition adopted in the emission inventory. Future investigations into the $\delta^{34}S$ of sulfur-containing emission sources and measurements of isotopic fractionation during combustion, ~~gas desulfurization~~FGD, and multiphase chemical reactions will help improve the simulation. ~~The isotope-enabled models illustrate~~By explicitly resolving the dynamic isotopic evolution of ~~isotopes in~~ reactant reservoirs ~~and indicate~~, the isotope-enabled model further shows that the reservoir effect in open

systems is ~~found to be~~ less pronounced than ~~initially~~ estimated by the conventional Rayleigh equation. ~~The model can serve as~~Overall, by providing additional isotopic constraints, the model offers a ~~valuable tool~~framework for ~~a comprehensive understanding of the~~interpreting sulfur isotope ~~effect~~effects and ~~further reduce the~~for reducing uncertainties in sulfur chemistry and budgets ~~by providing additional isotopic constraints~~.

Code and data availability

The compiled observation data and model output in our work are available via Wei et al. (2024). The developed isotopic chemistry module is available on Zenodo as Wei, et al. (2025).

Supplement

Supporting descriptions of CTM and model configuration, the algorithm framework of the isotopic chemistry module, the derivation of the stable isotopic composition of the reservoir in open systems, additional data, figures, and tables are given in the Supporting Information.

Author contributions

L.W., Z.W. and P.F. designed research; L.W., X.C., J.L. and W.Y. developed the isotope-enabled model; L.W., X.C., Z.W., Y.C., D.L., H.D. and X.P. made a discussion on the algorithm; L.W. and X.C. performed the modeling experiments; L.W. analyzed the data and wrote the paper. All authors have approved the final version of the manuscript.

Competing interests

The contact author has declared that none of the authors has any competing interests.

Acknowledgments

L. Wei thanks China Postdoctoral Science Foundation (Grant No. 2018M641451) and Chinese Scholarship Council for financial support of her research at the Max Planck Institute for Chemistry. The authors would like to thank Prof. Huiming Bao of International Center for Isotope Effects Research (ICIER) of Nanjing University for helpful discussions on topics related to this work.

Financial support

This research has been supported by the National Key R&D Program of China (Grant No. 2023YFC3710600) and the National Natural Science Foundation of China (Grant No. 41907201, 42377105).

References

~~IPCC, 2023: Climate Change 2023: Synthesis Report. A Report of the Intergovernmental Panel on Climate Change. Contribution of Working Groups I, II and III to the Sixth Assessment Report of the Intergovernmental Panel on Climate Change [Core Writing Team, H. Lee and J. Romero (eds.)], IPCC, Geneva, Switzerland, pp. 35-115., doi: 10.59327/IPCC/AR6-9789291691647,~~

Alexander, B., Park, R. J., Jacob, D. J., and Gong, S.: Transition metal-catalyzed oxidation of atmospheric sulfur: Global implications for the sulfur budget, J. Geophys. Res-Atmos., 114, 10.1029/2008jd010486, 2009.

Berglen, T. F., Berntsen, T. K., Isaksen, I. S., and Sundet, J. K.: A global model of the coupled sulfur/oxidant chemistry in the troposphere: The sulfur cycle, Journal of Geophysical Research: Atmospheres, 109, 2004.

Chen, H., Wang, Z., Li, J., Tang, X., Ge, B., Wu, X., Wild, O., and Carmichael, G.: GNAQPMS-Hg v1. 0, a global nested atmospheric mercury transport model: Model description, evaluation and application to trans-boundary transport of Chinese anthropogenic emissions, Geoscientific Model Development, 8, 2857-2876, 2015.

Chen, S. L., Guo, Z. Y., Guo, Z. B., Guo, Q. J., Zhang, Y. L., Zhu, B., and Zhang, H. X.: Sulfur isotopic fractionation and its implication: Sulfate formation in $PM_{2.5}$ and coal combustion under different conditions, Atmospheric Research, 194, 142-149, 10.1016/j.atmosres.2017.04.034, 2017.

Chen, X., Wang, Z., Li, J., and Yu, F.: Development of a regional chemical transport model with size-resolved aerosol microphysics and its application on aerosol number concentration simulation over China, Sola, 10, 83-87, 2014.

设置了格式: 下标

Chen, X., Yang, W., Wang, Z., Li, J., Hu, M., An, J., Wu, Q., Wang, Z., Chen, H., and Wei, Y.: Improving new particle formation simulation by coupling a volatility-basis set (VBS) organic aerosol module in NAQPMS+ APM, Atmos. Environ., 204, 1-11, 2019.

Chen, X., Yu, F., Yang, W., Sun, Y., Chen, H., Du, W., Zhao, J., Wei, Y., Wei, L., and Du, H.: Global–regional nested simulation of particle number concentration by combing microphysical processes with an evolving organic aerosol module, Atmos. Chem. Phys., 21, 9343-9366, 2021.

Cheng, Y., Zheng, G., Wei, C., Mu, Q., Zheng, B., Wang, Z., Gao, M., Zhang, Q., He, K., and Carmichael, G.: Reactive nitrogen chemistry in aerosol water as a source of sulfate during haze events in China, Sci. Adv., 2, e1601530, 2016.

Crippa, M., Guizzardi, D., Butler, T., Keating, T., Wu, R., Kaminski, J., Kuenen, J., Kurokawa, J., Chatani, S., and Morikawa, T.: The HTAP_v3 emission mosaic: merging regional and global monthly emissions (2000–2018) to support air quality modelling and policies, Earth System Science Data (Online), 15, 2023.

De Laeter, J. R., Bohlke, J. K., De Bievre, P., Hidaka, H., Peiser, H. S., Rosman, K. J. R., and Taylor, P. D. P.: Atomic weights of the elements: Review 2000 - (IUPAC technical report), Pure and Applied Chemistry, 75, 683-800, 10.1351/pac200375060683, 2003.

Derda, M., Grzegorz Chmielewski, A., and Licki, J.: Sulphur isotope compositions of components of coal and S-isotope fractionation during its combustion and flue gas desulphurization, Isotopes in Environmental and Health Studies, 43, 57-63, 2007.

Ding, S., Chen, Y., Li, Q., and Li, X.-D.: Using Stable Sulfur Isotope to Trace Sulfur Oxidation Pathways during the Winter of 2017–2019 in Tianjin, North China, International Journal of Environmental Research and Public Health, 19, 10966, 2022.

Ding, T., Valkiers, S., Kipphardt, H., De Bievre, P., Taylor, P. D. P., Gonfiantini, R., and Krouse, R.: Calibrated sulfur isotope abundance ratios of three IAEA sulfur isotope reference materials and V-CDT with a reassessment of the atomic weight of sulfur, Geochimica Et Cosmochimica Acta, 65, 2433-2437, 10.1016/s0016-7037(01)00611-1, 2001.

Ding, X., Li, Q., Wu, D., Wang, X., Li, M., Wang, T., Wang, L., and Chen, J.: Direct observation of sulfate explosive growth in wet plumes emitted from typical coal-fired stationary sources, Geophys. Res. Lett., 48, e2020GL092071, 2021.

Fan, M.-Y., Zhang, Y.-L., Lin, Y.-C., Li, J., Cheng, H., An, N., Sun, Y., Qiu, Y., Cao, F., and Fu, P.: Roles of sulfur oxidation pathways in the variability in stable sulfur isotopic composition of sulfate aerosols at an urban site in Beijing, China, Environ. Sci. Technol. Lett., 7, 883-888, 2020.

Fang, H. and Michalski, G.: Assessing the roles emission sources and atmospheric processes play in simulating δ 15 N of atmospheric NO x and NO 3− using CMAQ (version 5.2. 1) and SMOKE (version 4.6), Geoscientific Model Development, 15, 4239-4258, 2022.

Feng, X., Chen, Y., Liu, Z., Feng, Y., Du, H., Mu, Y., and Chen, J.: Exploring the influence of 34S fractionation from emission sources and SO2 atmospheric oxidation on sulfate source apportionment based on hourly resolution δ34S-SO2/SO42-, Journal of Geophysical Research: Atmospheres, e2023JD038595, 2023.

Fountoukis, C. and Nenes, A.: ISORROPIA II: a computationally efficient thermodynamic equilibrium model for K^+–Ca^{2+}–Mg^{2+}–NH_4^+–Na^+–SO_4^{2-}–NO_3^-–Cl^-–H_2O aerosols, Atmos. Chem. Phys., 7, 4639-4659, 2007.

951 Gromov, S., Jöckel, P., Sander, R., and Brenninkmeijer, C. A.: A kinetic chemistry tagging
952 technique and its application to modelling the stable isotopic composition of atmospheric trace
953 gases, Geoscientific Model Development, 3, 337-364, 2010.
954 Guan, Z. X. and Liu, Y.: How to estimate isotope fractionations of a Rayleigh-like but diffusion-
955 limited disequilibrium process?, Acta Geochimica, 42, 24-37, 2023.
956 Guo, Z., Shi, L., Chen, S., Jiang, W., Wei, Y., Rui, M., and Zeng, G.: Sulfur isotopic fractionation
957 and source appointment of $PM_{2.5}$ in Nanjing region around the second session of the Youth
958 Olympic Games, Atmospheric Research, 174, 9-17, 2016.
959 Han, X., Lang, Y., Guo, Q., Li, X., Ding, H., and Li, S.: Enhanced Oxidation of SO2 by H2O2 During
960 Haze Events: Constraints From Sulfur Isotopes, Journal of Geophysical Research: Atmospheres,
961 127, e2022JD036960, 2022.
962 Han, X., Guo, Q., Liu, C., Fu, P., Strauss, H., Yang, J., Hu, J., Wei, L., Ren, H., and Peters, M.: Using
963 stable isotopes to trace sources and formation processes of sulfate aerosols from Beijing, China,
964 Sci. Rep., 6, 2016a.
965 Han, X., Guo, Q., Liu, C., Strauss, H., Yang, J., Hu, J., Wei, R., Tian, L., Kong, J., and Peters, M.:
966 Effect of the pollution control measures on $PM_{2.5}$ during the 2015 China Victory Day Parade:
967 Implication from water-soluble ions and sulfur isotope, Environ. Pollut., 218, 230-241, 2016b.
968 Han, X., Guo, Q., Strauss, H., Liu, C., Hu, J., Guo, Z., Wei, R., Peters, M., Tian, L., and Kong, J.:
969 Multiple sulfur isotope constraints on sources and formation processes of sulfate in Beijing
970 PM2. 5 aerosol, Environ. Sci. Technol., 51, 7794-7803, 2017.

971 Harris, E., Sinha, B., Hoppe, P., and Ono, S.: High-Precision Measurements of ^{33}S and ^{34}S
972 Fractionation during SO_2 Oxidation Reveal Causes of Seasonality in SO_2 and Sulfate Isotopic
973 Composition, Environ. Sci. Technol., 47, 12174-12183, 10.1021/es402824c, 2013.
974 Harris, E., Sinha, B., Hoppe, P., Foley, S., and Borrmann, S.: Fractionation of sulfur isotopes
975 during heterogeneous oxidation of SO_2 on sea salt aerosol: a new tool to investigate non-sea
976 salt sulfate production in the marine boundary layer, Atmos. Chem. Phys., 12, 4619-4631,
977 10.5194/acp-12-4619-2012, 2012a.
978 Harris, E., Sinha, B., Foley, S., Crowley, J. N., Borrmann, S., and Hoppe, P.: Sulfur isotope
979 fractionation during heterogeneous oxidation of SO_2 on mineral dust, Atmos. Chem. Phys., 12,
980 4867-4884, 10.5194/acp-12-4867-2012, 2012b.
981 Harris, E., Sinha, B., Hoppe, P., Crowley, J. N., Ono, S., and Foley, S.: Sulfur isotope fractionation
982 during oxidation of sulfur dioxide: gas-phase oxidation by OH radicals and aqueous oxidation by
983 H_2O_2, O_3 and iron catalysis, Atmos. Chem. Phys., 12, 407-423, 10.5194/acp-12-407-2012, 2012c.
984 Hoefs, J.: Stable isotope geochemistry, Seventh, Springer Science & Business Media,
985 10.1007/978-3-319-19716-6, 2015.
986 Hoefs, J. and Harmon, R.: The Earth's atmosphere–A stable isotope perspective and review,
987 Applied Geochemistry, 143, 105355, 2022.
988 Hong, Y., Zhang, H., and Zhu, Y.: Sulfur isotopic characteristics of coal in China and sulfur
989 isotopic fractionation during coal-burning process, Chinese Journal of Geochemistry, 12, 51-59,
990 1993.

Itahashi, S., Hattori, S., Ito, A., Sadanaga, Y., Yoshida, N., and Matsuki, A.: Role of Dust and Iron Solubility in Sulfate Formation during the Long-Range Transport in East Asia Evidenced by 17O-Excess Signatures, Environ. Sci. Technol., 56, 13634-13643, 2022.

Li, J., Chen, X., Wang, Z., Du, H., Yang, W., Sun, Y., Hu, B., Li, J., Wang, W., and Wang, T.: Radiative and heterogeneous chemical effects of aerosols on ozone and inorganic aerosols over East Asia, Sci. Total Environ., 622, 1327-1342, 2018.

Lin, Y.-C., Yu, M., Xie, F., and Zhang, Y.: Anthropogenic emission sources of sulfate aerosols in Hangzhou, East China: insights from isotope techniques with consideration of fractionation effects between gas-to-particle transformations, Environ. Sci. Technol., 56, 3905-3914, 2022.

Liu, T. and Abbatt, J. P.: Oxidation of sulfur dioxide by nitrogen dioxide accelerated at the interface of deliquesced aerosol particles, Nature Chemistry, 13, 1173-1177, 2021.

Liu, X.: Progress of desulfurization and denitration technology of flue gas in China, IOP Conference Series: Earth and Environmental ~~Science, 042010,~~ Science2019.

Mariotti, A., Germon, J., Hubert, P., Kaiser, P., Letolle, R., Tardieux, A., and Tardieux, P.: Experimental determination of nitrogen kinetic isotope fractionation: some principles; illustration for the denitrification and nitrification processes, Plant and soil, 62, 413-430, 1981.

Oduro, H., Van Alstyne, K. L., and Farquhar, J.: Sulfur isotope variability of oceanic DMSP generation and its contributions to marine biogenic sulfur emissions, Proc. Natl. Acad. Sci. U. S. A., 109, 9012-9016, 2012.

Seinfeld, J. H. and Pandis, S. N.: Atmospheric Chemistry and Physics: From Air Pollution to Climate Change, Third, John Wiley & Sons, Inc., Hoboken, New Jersey, 1120 pp.2016.

Shao, J., Chen, Q., Wang, Y., Lu, X., He, P., Sun, Y., Shah, V., Martin, R. V., Philip, S., Song, S., Zhao, Y., Xie, Z., Zhang, L., and Alexander, B.: Heterogeneous sulfate aerosol formation mechanisms during wintertime Chinese haze events: air quality model assessment using observations of sulfate oxygen isotopes in Beijing, Atmos. Chem. Phys., 19, 6107-6123, 10.5194/acp-19-6107-2019, 2019.

Song, S., Gao, M., Xu, W., Shao, J., Shi, G., Wang, S., Wang, Y., Sun, Y., and McElroy, M. B.: Fine-particle pH for Beijing winter haze as inferred from different thermodynamic equilibrium models, Atmos. Chem. Phys., 18, 7423-7438, 10.5194/acp-18-7423-2018, 2018.

Song, Z., Sun, R., and Zhang, Y.: Modeling mercury isotopic fractionation in the atmosphere, Environ. Pollut., 307, 119588, 2022.

Stockwell, W. R., Kirchner, F., Kuhn, M., and Seefeld, S.: A new mechanism for regional atmospheric chemistry modeling, Journal of Geophysical Research: Atmospheres, 102, 25847-25879, 1997.

Sun, X., Jiang, H., and Bao, H.: Triple oxygen isotope composition of combustion sulfate, Atmos. Environ., 314, 120095, 2023.

~~Tao, W., Su, H., Zheng, G., Wang, J., Wei, C., Liu, L., Ma, N., Li, M., Zhang, Q., and Pöschl, U.: Aerosol pH and chemical regimes of sulfate formation in aerosol water during winter haze in the North China Plain, Atmos. Chem. Phys., 20, 11729-11746, 2020.~~

~~Toyoda, S., Mutobe, H., Yamagishi, H., Yoshida, N., and Tanji, Y.: Fractionation of N_2O isotopomers during production by denitrifier, Soil Biology and Biochemistry, 37, 1535-1545, 2005.~~

Van Breukelen, B. M.: Extending the Rayleigh equation to allow competing isotope fractionating pathways to improve quantification of biodegradation, Environ. Sci. Technol., 41, 4004-4010, 2007.

Wang, G., Zhang, R., Gomez, M. E., Yang, L., Levy Zamora, M., Hu, M., Lin, Y., Peng, J., Guo, S., and Meng, J.: Persistent sulfate formation from London Fog to Chinese haze, Proc. Natl. Acad. Sci. U. S. A., 113, 13630-13635, 2016.

Wang, W., Liu, M., Wang, T., Song, Y., Zhou, L., Cao, J., Hu, J., Tang, G., Chen, Z., Li, Z., Xu, Z., Peng, C., Lian, C., Chen, Y., Pan, Y., Zhang, Y., Sun, Y., Li, W., Zhu, T., Tian, H., and Ge, M.: Sulfate formation is dominated by manganese-catalyzed oxidation of SO2 on aerosol surfaces during haze events, Nature communications, 12, 1993-1993, 10.1038/s41467-021-22091-6, 2021.

Wang, Z., Maeda, T., Hayashi, M., Hsiao, L.-F., and Liu, K.-Y.: A nested air quality prediction modeling system for urban and regional scales: Application for high-ozone episode in Taiwan, Water, Air, and Soil Pollution, 130, 391-396, 2001.

Wei, L~~., Yue, S., Zhao, W., Yang, W., Zhang, Y., Ren, L., Han, X., Guo, Q., Sun, Y., and Wang, Z.: Stable sulfur isotope ratios and chemical compositions of fine aerosols (PM2. 5) in Beijing, China, Sci. Total Environ., 633, 1156-1164, 2018a~~.: The dataset of compiled observed and simulated sulfur isotopic composition ($\delta^{34}S\_SO_2$, $\delta^{34}S\_SO_4^{2-}$) across Eastern China's cities, Zenodo [dataset], https://doi.org/10.5281/zenodo.14357423, 2024.

Wei, L.: Isotopic Chemistry Module Developed and Coupled with NAQPMS Model, Zenodo, https://doi.org/10.5281/zenodo.14724954, 2025.

Wei, L., Yue, S., Zhao, W., Yang, W., Zhang, Y., Ren, L., Han, X., Guo, Q., Sun, Y., Wang, Z., and Fu, P.: Stable sulfur isotope ratios and chemical compositions of fine aerosols ($PM_{2.5}$) in Beijing,

China, Sci. Total Environ., 633, 1156-1164, ~~https://doi.org/10.1016/j.scitotenv.2018.03.153,~~ ~~2018b~~10.1016/j.scitotenv.2018.03.153, 2018.

Wei, Y., Chen, X., Chen, H., Li, J., Wang, Z., Yang, W., Ge, B., Du, H., Hao, J., and Wang, W.: IAP-AACM v1. 0: a global to regional evaluation of the atmospheric chemistry model in CAS-ESM, Atmos. Chem. Phys., 19, 8269-8296, 2019.

Yang, D. A., Bardoux, G., Assayag, N., Laskar, C., Widory, D., and Cartigny, P.: Atmospheric SO_2 oxidation by NO_2 plays no role in the mass independent sulfur isotope fractionation of urban aerosols, Atmos. Environ., 193, 109-117, 2018.

Yang, W., Li, J., Wang, W., Li, J., Ge, M., Sun, Y., Chen, X., Ge, B., Tong, S., and Wang, Q.: Investigating secondary organic aerosol formation pathways in China during 2014, Atmos. Environ., 213, 133-147, 2019.

Zaveri, R. A. and Peters, L. K.: A new lumped structure photochemical mechanism for large-scale applications, Journal of Geophysical Research: Atmospheres, 104, 30387-30415, 1999.

Zhang, Z., Wang, W., Cheng, M., Liu, S., Xu, J., He, Y., and Meng, F.: The contribution of residential coal combustion to $PM_{2.5}$ pollution over China's Beijing-Tianjin-Hebei region in winter, Atmos. Environ., 159, 147-161, https://doi.org/10.1016/j.atmosenv.2017.03.054, 2017.

Zheng, M., Song, D., Zhang, D., and Zhao, Z.: Variability of sulfur and oxygen isotope values within wet precipitation and its correlation with diminished anthropogenic sulfur dioxide (SO_2) emission, Atmos. Environ., 317, 120185, 2024.

设置了格式: 下标

Supporting Information for

Advancing Isotope-Enabled Model for Comprehensive Understanding of Atmospheric Sulfur Isotope Effects: ~~Revealing~~Demonstrating the Overlooked Isotopic Fractionation During Combustion and Flue Gas Desulfurization

Lianfang Wei[1,2,3], Xueshun Chen[1], Wenyi Yang[4], Zhe Wang[1], Jie Li[1], Di ~~Liu~~[1]Liu[5], Huiyun Du[1], Xiaole Pan[1], Yafang Cheng[3], Pingqing ~~Fu~~[5]Fu[6], Zifa Wang[1,~~6~~7*]*

[1] State Key Laboratory of Atmospheric ~~Boundary Layer Physics~~Environment and ~~Atmospheric Chemistry~~Extreme Meteorology, Institute of Atmospheric Physics, Chinese Academy of Sciences, Beijing 100029, China

[2] Chinese Research Academy of Environmental Sciences, Beijing 100012, China

[3] Aerosol Chemistry Department, Max Planck Institute for Chemistry, Mainz, Germany

[4] Center of Air Quality Simulation and System Analysis, Chinese Academy of Environmental Planning, Beijing 100012, China

[~~5~~5] State Key Laboratory of Regional Environment and Sustainability, School of Environment, Beijing Normal University, Beijing 100875, China

[6] Institute of Surface-Earth System Science, School of Earth System Science, Tianjin University, Tianjin 300072, China

[~~6~~7] University of Chinese Academy of Sciences, Beijing, 100049, China

Corresponding author: Pingqing Fu (fupingqing@tju.edu.cn), Zifa Wang (zifawang@mail.iap.ac.cn)

This supporting information document contains 19 pages with detailed descriptions of CTM and model configuration, the algorithm framework of the isotopic chemistry module, the derivation of the stable isotopic composition of a reservoir in open systems, additional data, 2 tables, 3 figures, and references.

样式定义: 正文: 字体: (中文) 宋体
样式定义: 标题 1: 字体: (默认) 等线 Light, (中文) 等线 Light, 字体颜色: 自定义颜色(RGB(47,84,150))
样式定义: 标题 2: 字体: (默认) 等线 Light, (中文) 等线 Light, 字体颜色: 自定义颜色(RGB(47,84,150))
样式定义: 正文文本: 字体: (中文) 宋体
样式定义: 批注框文本: 字体: (中文) 宋体
样式定义: 页脚: 字体: (中文) 宋体
样式定义: 页眉: 字体: (中文) 宋体
样式定义: 要点
样式定义: 访问过的超链接
样式定义: 超链接
样式定义: AF_Title_Running_Head: 字体: (中文) 宋体
样式定义: AI_Received_Date: 字体: (中文) 宋体
样式定义: BA_Title: 字体: (中文) 宋体
样式定义: BB_Author_Name: 字体: (中文) 宋体
样式定义: BC_Author_Address: 字体: (中文) 宋体
样式定义: BD_Abstract: 字体: (中文) 宋体
样式定义: BE_Author_Biography: 字体: (中文) 宋体
样式定义: BG_Keywords: 字体: (中文) 宋体
样式定义: BH_Briefs: 字体: (中文) 宋体
样式定义: BI_Email_Address: 字体: (中文) 宋体
样式定义: Default
样式定义: FA_Author_Info_Subtitle: 字体: (中文) 宋体
样式定义: FA_Corresponding_Author_Footnote: 字体: (中文) 宋体
样式定义: FC_Chart_Footnote: 字体: (中文) 宋体
样式定义: FD_Scheme_Footnote: 字体: (中文) 宋体
样式定义: FE_Table_Footnote: 字体: (中文) 宋体
样式定义: SN_Synopsis_TOC: 字体: (中文) 宋体
样式定义: Style FA_Corresponding_Author_Footnote + 7 pt: 字体: (中文) 宋体
样式定义: TA_Main_Text: 字体: (中文) 宋体
样式定义: TC_Table_Body: 字体: (中文) 宋体
样式定义: TD_Acknowledgments: 字体: (中文) 宋体
样式定义: TE_Supporting_Information: 字体: (中文) 宋体
样式定义: TF_References_Section: 字体: (中文) 宋体
样式定义: VB_Chart_Title: 字体: (中文) 宋体
样式定义: EndNote Bibliography Title: 字体: (中文) 宋体, 检查拼写和语法
样式定义: EndNote Bibliography: 字体: (中文) 宋体, 检查拼写和语法
样式定义: 无间隔: 字体: (中文) 宋体
设置了格式: 字体颜色: 黑色
带格式的: 行距: 单倍行距
带格式的: 行距: 单倍行距
设置了格式: 字体颜色: 黑色
带格式的: 周围环绕

Text S1 The description of CTMs and model configuration. The three-dimensional atmospheric chemical transport model (CTMs) solves the continuity equation for the chemical species for representing its entire cycle in the atmosphere, including emission, transport (e.g. diffusion, advection), chemical production/loss, dry and wet deposition processes. The general Eulerian form of the continuity equation can be expressed mathematically by

$$\frac{\partial \bar{c}}{\partial t} = -\nabla \cdot (\bar{c}\bar{U}) + \nabla \cdot (K\nabla \cdot \bar{c}) + [\frac{\partial \bar{c}}{\partial t}]_{Emis} + [\frac{\partial \bar{c}}{\partial t}]_{Chem} - [\frac{\partial \bar{c}}{\partial t}]_{Dry} - [\frac{\partial \bar{c}}{\partial t}]_{Wet}$$

$$\frac{\partial \bar{c}}{\partial t} = -\nabla \cdot (\bar{c}\bar{U}) + \nabla \cdot (K\nabla \cdot \bar{c}) + [\frac{\partial \bar{c}}{\partial t}]_{Emis} + [\frac{\partial \bar{c}}{\partial t}]_{Chem} - [\frac{\partial \bar{c}}{\partial t}]_{Dry} - [\frac{\partial \bar{c}}{\partial t}]_{Wet}$$

(S1)

where ~~$\bar{c}\ell$~~ is the time-averaged concentration of the chemical species of interest. The term on the left side is the temporal change of concentration. The first two terms on the right side are advection, and turbulent diffusion of the time-averaged flux, the last four terms represent the emission intensity, time-averaged rate of chemical interactions (including production and loss process), dry deposition, and wet scavenge. $\nabla = (\partial/\partial x, \partial/\partial y, \partial/\partial z)$ is the gradient vector, U = (u, v, w) is the local wind velocity vector, and K is a 3×3 matrix with zero values for the non-diagonal elements and with diagonal elements K_x, K_y, K_z representing the turbulent diffusion coefficients in each transport direction.

The model is initialized using gridded meteorological and emission input. The meteorological field is processed through the interpolation of NCEP FNL (Final) Operational Global Analysis and forecast dataset on 0.25° × 0.25° grids~~, employing the WRF (Weather Research and Forecast model, version 3.9).~~, employing the WRF (Weather Research and Forecast model, version 3.9). Anthropogenic emissions, including SO_2, NO_x, NH_3, CO, VOCs, black carbon, and organic carbon, are obtained

设置了格式: 字体颜色: 黑色

设置了格式: 字体颜色: 黑色

设置了格式: 字体颜色: 黑色

设置了格式: 字体颜色: 黑色

带格式的: 周围环绕

from the fusion of Hemispheric Transport of Air Pollution version-2 (HTAPv2) at a 1° horizontal resolution for the year 2010 (Janssens-Maenhout et al., 2015), and the Multi-resolution Emission Inventory for China (MEIC) at a 0.1°× 0.1° horizontal resolution for the year 2015 (Li et al., 2017). The emission inventory for the Chinese region is overwritten with the MEIC. The online mineral dust is based on the wind erosion model developed by Wang et al. (2000) and the sea salt emissions parameterizations are referenced from Athanasopoulou et al. (2008), respectively.

The Rapid Radiative Transfer Model for General Circulation Model (RRTMG) scheme is employed for the computation of longwave and shortwave atmospheric radiative fluxes and heating rates (Pincus et al., 2003). The Madronich F-TUV (Fast Tropospheric Ultraviolet-Visible) scheme is utilized to estimate the photolysis rate. The WSM3 scheme (Hong et al., 2004) is selected for microphysics schemes. For the surface layer and boundary layer evaluations, the Monin-Obukhov scheme (Monin and Obukhov, 1954) and the Yonsei University (YSU) scheme (Hong et al., 2006) are chosen, respectively.

The Carbon Bond Mechanism version Z (CBM-Z) is employed for the gas-phase chemistry scheme (Zaveri and Peters, 1999). The aqueous chemistry module is taken from Regional Acid Deposition Model (RADM2) (Stockwell et al., 1997), including sulfur chemistry and a simple mechanism for wet scavenging. The dry deposition process is parameterized through the calculation of deposition velocity, employing the resistance model approach developed by Zhang et al. (2003). Recently, the Global Nested Grid Air Quality Prediction Model System (GNAQPMS) has been coupled with the CAS earth system model (CAS-ESM) (Wei et al., 2019). It shows good performance on the global budgets and spatial distribution of major atmospheric species, as validated against

带格式的: 周围环绕

field observations and other model results. The oxidation processes of S(IV) to S(VI) involve gas-phase oxidation by SO_2 and OH radical, as well as aqueous phase oxidation through dissoluble S(IV) with O_3, H_2O_2, NO_2, and proxy acetic acid (CH_3OOH), along with transition metal-catalyzed O_2 in cloud water. The oxidation of S(IV) species by dissolved NO_2 is also incorporated into the sulfur aqueous chemistry, referring to the kinetic parameters proposed by Cheng et al. (2016). The bulk cloud water pH is iteratively calculated online using the electroneutrality equation, considering concentrations of anions (sulfate, sulfite, nitrate, carbonate, formic acid) and cations (NH_4^+, Ca^{2+}, Mg^{2+}, Mn^{2+}, Fe^{3+}). Ion concentrations are determined based on Henry's law, dissociation equilibrium and ionization processes. Neutralized cations are mainly contributed by dust aerosol, with natural dust materials assumed to contain 10 wt% of Ca^{2+}, 3 wt% of Mg^{2+}, 0.5 wt% of Mn^{2+} and 0.5 wt% of Fe^{3+} (Wang et al., 2002). The gas–particle partitioning of inorganic aerosols and aerosol water content is simulated using the improved thermodynamic equilibrium module ISORROPIA II (Fountoukis and Nenes, 2007; Song et al., 2018). Refer to Table S2 for a comprehensive description of the model configuration.

The current implementation of the isotopic chemistry module relies on several assumptions. (1) The pollutants and cloud water are uniformly distributed within the grid cell. (2) During wet scavenging and dry deposition, no isotopic fractionation occurs, the small mass change due to isotopic substation is insignificant relative to the mass of particle, therefore, we apply the same K_j to ^{32}S and ^{34}S due to their similar molecular mass. (3) The model does not account for variations in isotopic composition from different emission sources. Instead, we focus on model's ability to reproduce the isotope effect, thus the isotopic composition of SO_2 and sulfate from emission sources

带格式的: 周围环绕

are simply set to 0‰. The treatment does not influence the comparison between simulated and observed sulfur isotope effect during oxidation processes.

Text S2 The algorithm framework of isotopic chemistry module

We initially track the net change of SO_2 and sulfate after gas-phase, heterogeneous, and cloud&aqueous chemistry module separately, and then determine the reaction fraction *f* of SO_2 with each specific oxidation pathway during every time step (Δt) to be used as input for the isotope chemistry module. At each time step, the temperature and the temperature-dependent isotopic fractionation factor at the grid cell are updated.

To reduce the effect of time-dependent Rayleigh equation with a large reaction fraction. The iterative time-splitting technique is employed. Within each sub-timestep, the reaction fraction is set at ~~1~~2%, and a repetition involves adding equal portions of a fresh mixture. Utilizing the input mass of sulfur-containing isotopologues $^{32}SO_2$ and $^{34}SO_2$ at the last time step as initial value, we calculate the isotope ratio of $^{32}SO_4^{2-}$ and $^{34}SO_4^{2-}$ in the product, as well as the isotope ratio of $^{32}SO_2$ and $^{34}SO_2$ in the remaining reactant based on Rayleigh equations. We then derive the net mass change of $^{32}SO_2$, $^{34}SO_2$, $^{32}SO_4^{2-}$ and $^{34}SO_4^{2-}$ using the isotopic mass balance at each sub-timestep, as expressed in the following equation.

$$\Delta MC(^{l}X)_t = \left(MC(^{h}X)_{S_{t-1}} - R(^{h}X/^{l}X)_{S_t} \times MC(^{l}X)_{S_{t-1}}\right) \Big/ \left(R(^{h}X/^{l}X)_{P_t} - R(^{h}X/^{l}X)_{S_t}\right)$$

$$\Delta MC(^{h}X)_t = R(^{h}X/^{l}X)_{P_t} \times \Delta MC(^{l}X)_t$$

$$\Delta MC(^{l}X)_t = \left(MC(^{h}X)_{S,t-1} - R_{S,t} \times MC(^{l}X)_{S,t-1}\right)/(R_{P,t} - R_{S,t}) \quad \text{(S2)}$$

设置了格式: 字体颜色: 黑色

带格式的: 周围环绕

$$\Delta MC\left({}^{h}X\right)_t = R_{S,t} \times \Delta MC\left({}^{l}X\right)_t \quad \text{(S3)}$$

Where $\Delta MC\left({}^{h}X\right)_t$ and $\Delta MC\left({}^{l}X\right)_t$ represent the change in molar mass of isotopologues containing ~~heavy~~ heavier isotope ${}^{h}X$ and ~~light~~lighter isotope ${}^{l}X$ ~~of element X~~ at time t during the chemical process, respectively. ~~$MC\left(\underline{{}^{h}X}\right)_{S_{t-1}}$~~ $MC\left({}^{h}X\right)_{S,t-1}$ and ~~$MC\left(\underline{{}^{l}X}\right)_{S_{t-1}}$~~ $\mathrm{MC}\left({}^{l}\mathrm{X}\right)_{\mathrm{S,t\text{-}1}}$ represent the molar mass of reactant S containing ~~heavy~~heavier isotope ${}^{h}X$ and ~~light~~lighter isotope ${}^{l}X$ ~~of element X~~ at time t-1, respectively.

During each sub-timestep, the isotope ratio of the substrate is updated with the new mixing, and the isotope ratio of the accumulated product is weighted with the molar mass and isotope ratio of the product at each sub-timestep. An iterative loop is executed for the above steps.

~~Text S3 The derivation of stable isotopic composition~~ of a reservoir in open systems.

We consider a reservoir that loses material due to any physicochemical process with isotopic fractionation at a constant temperature. At any instant, the stable isotope ratio is given by

$$\mathrm{R} = \frac{N^*}{N} \quad \text{~~...(S1)~~}$$

$$R = \frac{N\left({}^{h}X\right)}{N\left({}^{l}X\right)} \quad \text{(S4)}$$

where $N\left({}^{h}X\right)$ and $N\left({}^{l}X\right)$ represent the atomic abundances of the heavier stable isotope ($ {}^{h}X$) and lighter stable isotope ($ {}^{l}X$), respectively.

Taking the logarithm of both sides of ~~eq. (S1~~Equation (S4)

$$\ln R = \ln N^* - \ln N \quad \text{~~...(S2)~~}$$

$$lnR = ln\,N\left({}^{h}X\right) - lnN\left({}^{l}X\right) \quad \text{(S5)}$$

设置了格式: 字体颜色: 黑色
设置了格式: 字体颜色: 黑色
设置了格式: 字体颜色: 黑色
设置了格式: 字体颜色: 黑色
设置了格式: 字体颜色: 黑色
设置了格式: 字体颜色: 黑色
设置了格式: 字体颜色: 黑色
设置了格式: 字体颜色: 黑色
设置了格式: 字体颜色: 黑色
设置了格式: 字体颜色: 黑色
设置了格式: 字体颜色: 黑色
设置了格式: 字体颜色: 黑色
设置了格式: 字体颜色: 黑色
设置了格式: 字体颜色: 黑色
设置了格式: 字体颜色: 黑色
设置了格式: 字体颜色: 黑色
设置了格式: 字体颜色: 黑色
设置了格式: 字体颜色: 黑色
设置了格式: 字体: 非倾斜, 字体颜色: 黑色
设置了格式: 字体颜色: 黑色
设置了格式: 字体颜色: 黑色
设置了格式: 字体颜色: 黑色
设置了格式: 字体颜色: 黑色
设置了格式: 字体颜色: 黑色
设置了格式: 字体颜色: 黑色
设置了格式: 字体颜色: 黑色
设置了格式: 字体颜色: 黑色
设置了格式: 字体颜色: 黑色
设置了格式: 字体颜色: 黑色
带格式的: 周围环绕

After differentiating, eq. (S2Equation (S5) becomes

$$\frac{dR}{R} = \frac{dN^*}{N^*} - \frac{dN}{N} = \frac{dN^*}{NR} - \frac{dN}{N} \quad ...(S3)$$

$$\frac{dR}{R} = \frac{dN({}^{h}X)}{N({}^{h}X)} - \frac{dN({}^{l}X)}{N({}^{l}X)} = \frac{dN({}^{h}X)}{N({}^{l}X)\times R} - \frac{dN({}^{l}X)}{N({}^{l}X)} \quad (S6)$$

At any instant, let dN_e^* $dN({}^{h}X)_e$ and dN_e $dN({}^{l}X)_e$ are being lost and dN_r^* $dN({}^{h}X)_r$ and dN_r $dN({}^{l}X)_r$ are being added to the reservoir. So, the net change in N^* $N({}^{h}X)$ and N $N({}^{l}X)$ is

$$dN^* = dN_r^* - dN_e^*$$

$$dN = dN_r - dN_e \quad ...(S4), (S5)$$

$$dN({}^{h}X) = dN({}^{h}X)_r - dN({}^{h}X)_e \quad (S7)$$

$$dN({}^{l}X) = dN({}^{l}X)_r - dN({}^{l}X)_e \quad (S8)$$

Dividing eq. (S4Equation (S7) by eq. (S5Equation (S8)

$$\frac{dN^*}{dN} = \frac{dN_r^* - dN_e^*}{dN_r - dN_e} = \frac{\frac{dN_r^*}{dN_r}\times\frac{dN_r}{dN_e} - \frac{dN_e^*}{dN_e}}{\frac{dN_r}{dN_e} - 1} = \frac{\beta R_r - \alpha R}{\beta - 1} \quad ...(S6)$$

$$\frac{dN({}^{h}X)}{dN({}^{l}X)} = \frac{dN({}^{h}X)_r - dN({}^{h}X)_e}{dN({}^{l}X)_r - dN({}^{l}X)_e} = \frac{\frac{dN({}^{h}X)_r}{dN({}^{l}X)_r}\times\frac{dN({}^{l}X)_r}{dN({}^{l}X)_e} - \frac{dN({}^{h}X)_e}{dN({}^{l}X)_e}}{\frac{dN({}^{l}X)_r}{dN({}^{l}X)_e} - 1} = \frac{\beta R_r - \alpha R}{\beta - 1} \quad (S9)$$

Where α is defined as $(dN_e^*/dN_e)/(N^*/N)$, and $(dN({}^{h}X)_e/dN({}^{l}X)_e)/(N({}^{h}X)/N({}^{l}X))$, β is dN_r^*/dN_e $\frac{dN({}^{l}X)_r}{dN({}^{l}X)_e}$, the ratio of the amount of material added to that lost, and R_r is the stable isotope ratio of the reactant added to the reservoir during the interval.

Substituting the value of dN^* $dN({}^{h}X)$ from eq. Equation (S9) to Equation (S6) to eq. (S3)

$$\frac{dR}{R} = \left(\frac{\beta R_r - \alpha R}{\beta - 1}\right)\times\frac{dN}{NR} - \frac{dN}{N} = \frac{dN}{N}\times\left(\frac{\beta\frac{R_r}{R}}{\beta-1} - \frac{\alpha}{\beta-1} - 1\right) \quad ...(S7)$$

$$\frac{dR}{R} = \left(\frac{\beta R_r - \alpha R}{\beta - 1}\right)\times\frac{dN({}^{l}X)}{N({}^{l}X)\times R} - \frac{dN({}^{l}X)}{N({}^{l}X)} = \frac{dN({}^{l}X)}{N({}^{l}X)}\times\left(\frac{\beta\frac{R_r}{R}}{\beta-1} - \frac{\alpha}{\beta-1} - 1\right) \quad (S10)$$

设置了格式: 字体颜色: 黑色
设置了格式: 字体颜色: 黑色
设置了格式: 字体颜色: 黑色
设置了格式: 字体颜色: 黑色
设置了格式: 字体颜色: 黑色
设置了格式: 字体颜色: 黑色
设置了格式: 字体颜色: 黑色
设置了格式: 字体颜色: 黑色
设置了格式: 字体颜色: 黑色
设置了格式: 字体: 12 磅, 字体颜色: 黑色
设置了格式: 字体: 12 磅, 字体颜色: 黑色
设置了格式: 字体: 12 磅, 字体颜色: 黑色
设置了格式: 字体颜色: 黑色
设置了格式: 字体颜色: 黑色
设置了格式: 字体颜色: 黑色
设置了格式: 字体颜色: 黑色
设置了格式: 字体颜色: 黑色
设置了格式: 字体颜色: 黑色
设置了格式: 字体: (中文) +中文正文 (宋体), 字体颜色: 黑色
带格式的: 周围环绕

or

$$\frac{dR}{(\frac{\beta R_r}{\beta-1}-(\frac{\alpha}{\beta-1}+1)\times R)}=\frac{dN}{N}$$

~~...(S8)~~

$$\frac{dR}{\frac{\beta R_r}{\beta-1}-(\frac{\alpha}{\beta-1}+1)\times R}=\frac{dN(\ ^lX)}{N(\ ^lX)} \quad \text{(S11)}$$

Taking integration on both sides, the integral on the left side is in the form of $\int \frac{1}{A-B\times R}dR$.

$$\frac{1}{-(\frac{\alpha}{\beta-1}+1)}\int \frac{d\{\frac{\beta R_r}{\beta-1}-(\frac{\alpha}{\beta-1}+1)\times R\}}{\{\frac{\beta R_r}{\beta-1}-(\frac{\alpha}{\beta-1}+1)\times R\}}=\int\frac{dN}{N}$$

~~...(S9)~~

Using the substitution method, let $\mathrm{u}=\mathrm{A}-\mathrm{B}\times\mathrm{R}$, where $\mathrm{A}=\frac{\beta R_r}{\beta-1}$, and $\mathrm{B}=\frac{\alpha}{\beta-1}+1$.

Differentiating with respect to R yield du = −B dR, so $\mathrm{dR}=-\frac{1}{B}du$. Substituting into the integral ~~$\int \frac{1}{A-B\times R}dR$~~:

$$\int\frac{1}{u}\times(-\frac{1}{B})du=-\frac{1}{B}\int\frac{1}{u}du=-\frac{1}{B}=-\frac{1}{B}\ln|A-B*R| \quad \text{(S12)}$$

Then substitute the previously defined A and B back into the formula to obtain the final complete solution. The condition for integrating this equation is $\frac{\beta R_r}{\beta-1}\neq\left(\frac{\alpha}{\beta-1}+1\right)\times R$, it gives that $\frac{dN_r}{dN_e}\neq(\frac{\alpha-1}{\frac{R_r}{R}-1})$

$$\frac{1}{-(\frac{\alpha}{\beta-1}+1)}\int \frac{d\{\frac{\beta R_r}{\beta-1}-(\frac{\alpha}{\beta-1}+1)\times R\}}{\{\frac{\beta R_r}{\beta-1}-(\frac{\alpha}{\beta-1}+1)\times R\}}=\int\frac{dN(\ ^lX)}{N(\ ^lX)} \quad \text{(S13)}$$

Where $\frac{\beta R_r}{\beta-1}\neq(\frac{\alpha}{\beta-1}+1)\times R$, it gives that $\frac{dN(\ ^lX)_r}{dN(\ ^lX)_e}\neq(\frac{\alpha-1}{\frac{R_r}{R}-1})$.

At $\beta=1$, this equation is not solvable, hence first we take the case where $\beta\neq1$.

Case 1: on integrating ~~eq. (S8~~Equation (S13), we get

设置了格式: 字体颜色: 黑色

设置了格式: 字体颜色: 黑色

设置了格式: 字体: (中文) +中文正文 (宋体), 字体颜色: 黑色

设置了格式: 字体颜色: 黑色

设置了格式: 字体颜色: 黑色

设置了格式: 字体颜色: 黑色

带格式的: 周围环绕

$$\frac{1}{-(\frac{\alpha}{\beta-1}+1)} \times \ln\left\{\frac{\beta R_r}{\beta-1} - (\frac{\alpha}{\beta-1}+1) \times R\right\} = \ln N + k$$

...(S10)

$$\frac{1}{-(\frac{\alpha}{\beta-1}+1)} \times ln\left\{\frac{\beta R_r}{\beta-1} - (\frac{\alpha}{\beta-1} + 1) \times R\right\} = lnN(\ ^lX) + k \quad (S14)$$

After applying boundary conditions, at t=1, N=N$_0$,t$_0$, $N(\ ^lX)$=$N(\ ^lX)_0$, R=R$_0$, we evaluate *k* and substitute in eq. (S10Equation (S14)); we get

$$\frac{1}{-(\frac{\alpha}{\beta-1}+1)} \times \ln\left\{\frac{\{\frac{\beta R_r}{\beta-1} - (\frac{\alpha}{\beta-1}+1) \times R\}}{\{\frac{\beta R_r}{\beta-1} - (\frac{\alpha}{\beta-1}+1) \times R_0\}}\right\} = \ln\frac{N}{N_0} = \ln f$$

...(S11)

$$\frac{1}{-(\frac{\alpha}{\beta-1}+1)} \times ln\left\{\frac{\frac{\beta R_r}{\beta-1} - (\frac{\alpha}{\beta-1}+1) \times R}{\frac{\beta R_r}{\beta-1} - (\frac{\alpha}{\beta-1}+1) \times R_0}\right\} = ln\frac{N(\ ^lX)}{N(\ ^lX)_0} = lnf_{rem} \quad (S15)$$

Here $f f_{rem}$ is the fraction of the material left in the reservoir relative to the initial amount, which is difined as $(N^* + N)/(N_0^* + N_0)$.

Further simplifying eq. (S11Equation (S15)) becomes

$$\mathrm{R} = R_0 f^{-(\frac{\alpha}{\beta-1}+1)} + \frac{\beta}{\alpha+\beta-1} \times R_r \times \left[1 - f^{-(\frac{\alpha}{\beta-1}+1)}\right]$$

...(S12)

$$R = R_0 f_{rem}^{\ -(\frac{\alpha}{\beta-1}+1)} + \frac{\beta}{\alpha+\beta-1} \times R_r \times \left[1 - f_{rem}^{\ -(\frac{\alpha}{\beta-1}+1)}\right] \quad (S16)$$

or

$$\mathrm{R} = R_0 f^{\rho} + \frac{\beta}{\alpha+\beta-1} \times R_r \times [1 - f^{\rho}]$$

...(S13)

$$R = R_0 f_{rem}^{\ \rho} + \frac{\beta}{\alpha+\beta-1} \times R_r \times [1 - f_{rem}^{\ \rho}] \quad (S17)$$

Here $\rho = -(\frac{\alpha}{\beta-1}+1)$ $\rho = -(\frac{\alpha}{\beta-1}+1)$.

Substituting β=0, eq. (S13Equation (S17)) converts to the simple Rayleigh equation, which cross-checks the derivation.

$$\mathrm{R} = R_0 f^{(\alpha-1)}$$

...(S14)

设置了格式: 字体颜色: 黑色
设置了格式: 字体颜色: 黑色
设置了格式: 字体颜色: 黑色
设置了格式: 字体颜色: 黑色
设置了格式: 字体颜色: 黑色
设置了格式: 字体: (中文) +中文正文 (宋体), 字体颜色: 黑色
设置了格式: 字体颜色: 黑色
设置了格式: 字体颜色: 黑色
设置了格式: 字体: (中文) +中文正文 (宋体), 字体颜色: 黑色
设置了格式: 字体颜色: 黑色
带格式的: 周围环绕

$$R = R_0 {f_{rem}}^{(\alpha-1)} \quad \text{(S18)}$$

Case 2: When β=1, ~~dN = 0 hence~~$dN(\ ^{l}X) = 0$. Hence from ~~eq. (S5), $dN_r = dN_e$.~~

Equation (~~S3~~S8), $dN(\ ^{l}X)_r = dN(\ ^{l}X)_e$. Equation (S6) becomes

$$\mathrm{dR} = \frac{dN_r^* - dN_e^*}{N} = R_r\frac{dN_r}{N} - \alpha R\frac{dN_e}{N} = \left(\frac{R_r - \alpha R}{N}\right)dN_r = \left(\frac{R_r - \alpha R}{N_0}\right)dN_r$$

~~...(S15)~~

$$dR = \frac{\mathrm{dN}(\ ^{h}X)_r - \mathrm{dN}(\ ^{h}X)_e}{N(\ ^{l}X)} = R_r\frac{\mathrm{dN}(\ ^{l}X)_r}{N(\ ^{l}X)} - \alpha R\frac{\mathrm{dN}(\ ^{l}X)_e}{N(\ ^{l}X)}$$

$$= \left(\frac{R_r - \alpha R}{N(\ ^{l}X)}\right)dN(\ ^{l}X)_r = \left(\frac{R_r - \alpha R}{N(\ ^{l}X)_0}\right)dN(\ ^{l}X)_r \quad \text{(S19)}$$

After rearranging and integrating, this becomes

$$-\frac{1}{\alpha}\int\frac{d(R_r - \alpha R)}{R_r - \alpha R} = \frac{1}{N_0}\int dN_r$$

~~...(S16)~~

$$-\frac{1}{\alpha}\int\frac{d(R_r - \alpha R)}{R_r - \alpha R} = \frac{1}{N(\ ^{l}X)_0}\int dN(\ ^{l}X)_r \quad \text{(S20)}$$

After solving fully and applying boundary conditions as in the previous case, we get

$$\mathrm{R} = R_0 exp[-(\alpha N_r/N_0)] + (R_r/\alpha) \times \{1 - exp[-(\alpha N_r/N_0)]\}$$

~~...(S17)~~

$$R = R_0 exp\left[-\frac{\alpha N(\ ^{l}X)_r}{N(\ ^{l}X)_0}\right] + (R_r/\alpha) \times \left\{1 - exp\left[-\frac{\alpha N(\ ^{l}X)_r}{N(\ ^{l}X)_0}\right]\right\} \quad \text{(S21)}$$

Here ~~N_r~~$N(\ ^{l}X)_r$ indicates the total number of lighter ~~isotopeic~~isotopic molecules added thus far.

设置了格式: 字体颜色: 黑色
设置了格式: 字体颜色: 黑色
设置了格式: 字体颜色: 黑色
设置了格式: 字体颜色: 黑色
设置了格式: 字体颜色: 黑色
设置了格式: 字体颜色: 黑色
设置了格式: 字体颜色: 黑色
设置了格式: 字体颜色: 黑色
带格式的: 周围环绕

Table S1 Compiled observation data of $\delta^{34}S$ values of coal, sulfate aerosol, and wet precipitation across different Chinese provinces

Province	$\delta^{34}S$ of coal	$\delta^{34}S$ of wet precipitation	$\delta^{34}S$ of aerosol
Beijing	7.4±16.1	4.7±1.8	6.1±1.3
Tianjin			4.1±1.6
Inner Mongolia	0.8		
Heilongjiang	3.2±1.8		6.4
Liaoning	9.4±3.2		5.9
Jilin	1.7		8.1
Hebei	3.5±6.6		
Henan	6.4±1.0	2.1±2.3	
Shandong	7.6±2.9		
Gansu	7.3±3.5		
Zhejiang	4.0±1.5		6.2±2.7
Jiangsu	3.8±1.3		5.5±1.0
~~Anwei~~Anhui	3.8		
Fujian			3.5±1.1
Chongqing		4.3±1.1	
Jiangxi	-4.4±1.3		
Sichuan	8.8±1.3	3.9	
Shaanxi	7.9±4.6	12.3±1.1	
Shanxi	12.1±10.8		
Hubei	12.1		
Hunan	-6.6±5.7		
Guangdong	9.6±1.0		5.2±1.6
Guizhou	-7.5±0.1	-2.8±9.8	1.2
Yunnan	-0.7		

The dataset (Mean±std.) are compiled from references.

The compiled data from various Chinese provinces are cited from sources such as Beijing (Fan et al., 2020; Wei et al., 2018; Han et al., 2016b; Hong et al., 1993; Maruyama et al., 2000; Ohizumi et al., 1997; Mukai et al., 2001; Han et al., 2016a; Zhu et al., 2016), Tianjin (Han et al., 2022; Ding et al., 2022), Inner Mongolia (Hong et al., 1993), Heilongjiang (Hong et al., 1993; Ohizumi et al., 1997; Mukai et al., 2001), Liaoning (Hong et al., 1993; Maruyama et al., 2000; Ohizumi et al., 1997), Jilin

设置了格式: 字体颜色: 黑色
格式化表格
带格式的: 周围环绕

(Hong et al., 1993; Mukai et al., 2001), Hebei (Hong et al., 1993), Henan (Hong et al., 1993; Zheng et al., 2024), Shandong (Hong et al., 1993), Gansu (Xiao and Liu, 2011), Zhejiang (Hong et al., 1993; Lin et al., 2022), Jiangsu (Hong et al., 1993; Chen et al., 2017; Li et al., 2020; Maruyama et al., 2000; Mukai et al., 2001), ~~Anwei~~Anhui (Hong et al., 1993), Fujian (Lin et al., 2018), Chongqing (Xiao et al., 2009; Wu and Han, 2015), Jiangxi (Hong et al., 1993; Xiao and Liu, 2011; Xiao et al., 2009), Sichuan (Hong et al., 1993; Xiao et al., 2009), Shaanxi (Xiao and Liu, 2011; Bai and Wang, 2014), Shanxi (Xiao and Liu, 2011; Maruyama et al., 2000; Ohizumi et al., 1997), Hubei (Xiao and Liu, 2011), Hunan (Hong et al., 1993; Xiao and Liu, 2011), Guangdong (Lin et al., 2018)~~, Guizhou (Lin et al., 2018),~~ Guizhou (Hong et al., 1993; Mukai et al., 2001; Xiao et al., 2009; Xiao et al., 2014), Yunnan (Hong et al., 1993)

设置了格式: 字体颜色: 黑色

设置了格式: 字体颜色: 黑色

设置了格式: 字体颜色: 黑色

带格式的: 周围环绕

Table S2 The detailed information of model configurations

Module	Parameterizations/schemes
Input global analysis data	NCEP GDAS/FNL data
Gas-phase chemical mechanism	CBM-Z mechanism (Zaveri and Peters, 1999)
Aqueous-phase chemical mechanism and wet scavenge	RADM mechanism (Chang et al., 1987)
Anthropogenic emissions	HTAPv2 and MEIC
Dust, sea salt	wind erosion model (Wang et al., 2000) sea salt online parameterization (Athanasopoulou et al., 2008)
Photolysis scheme	Madronich F-TUV
Microphysics scheme	WSM3 (Hong et al., 2004)
Longwave radiation scheme	RRTM (Mlawer et al., 1997)
Shortwave radiation scheme	Dudhia scheme (Dudhia, 1989)
Surface layer	Monin-Obukhov (Janjic) scheme (Monin and Obukhov, 1954)
Land surface schemes	NOAH (Ek et al., 2003)
Planetary boundary layer physics	YSU scheme (Hong et al., 2006)
Cumulus	~~Kain-Fritsch scheme (Kain and Kain, 2004)~~Kain-Fritsch scheme (Kain, 2004)
Vertical layers	20

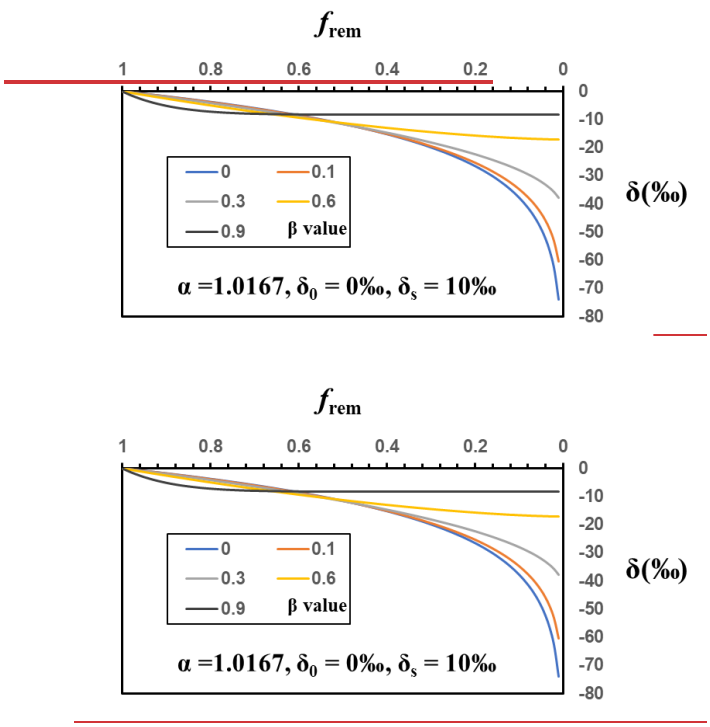

Figure S1. An example illustrating the change in isotopic composition (δ) of a reservoir related to the remaining fraction (f_{rem}) of the original material, considering various values of β, which represents the ratio of the instantaneous amount added to the removal during an infinitesimal time interval Δt (β ≠1). The isotopic composition of the external source (δ_s) is assumed to be 10‰, and the fractionation factor is set to 1.0167.

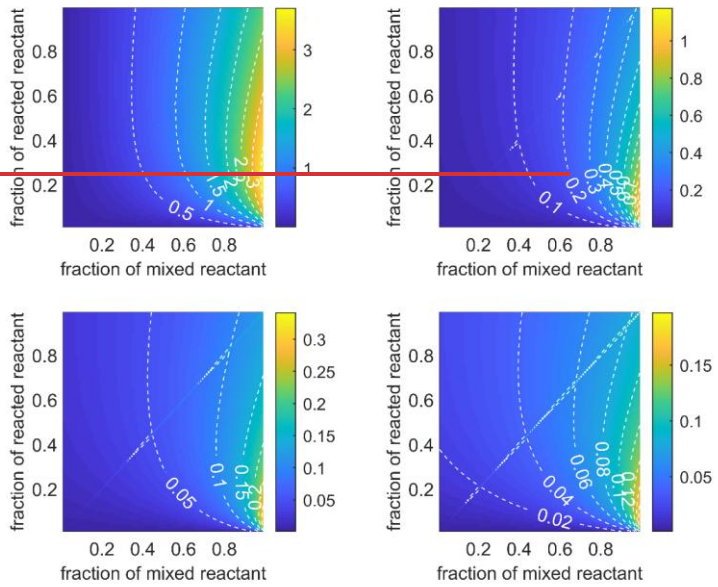

241

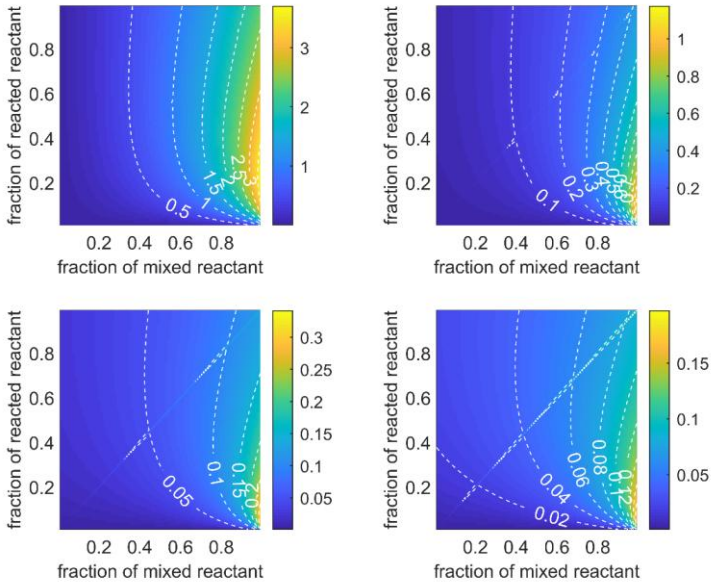

242

243 **Figure S2**. Simulation deviation of the isotopic composition of reservoir for varying

设置了格式: 字体颜色: 黑色

带格式的: 周围环绕

sub-steps (a) 1, (b) 10, (c) 50, and (d) 100, relative to reference simulation with integration method in the open system associated with simultaneous reaction and mixing processes. Each simulation involves the addition of a compound with an initial δ-value of 10.0‰ to the substrate (initially δ= 0‰), while the chemical reaction exhibits an isotopic effect with a fractionation factor of α= 1.0167. The fractions of added and removed products range from 1% to 99% of the initial amount of substrate and are uniformly divided at every time sub-step. The color scheme and contour lines illustrate the δ-value differences between the respective simulations and the referenced simulation.

带格式的: 周围环绕

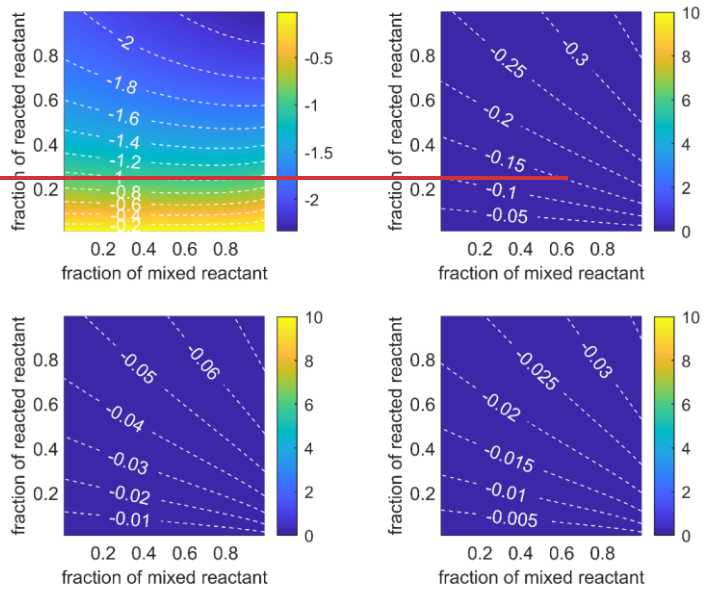

254

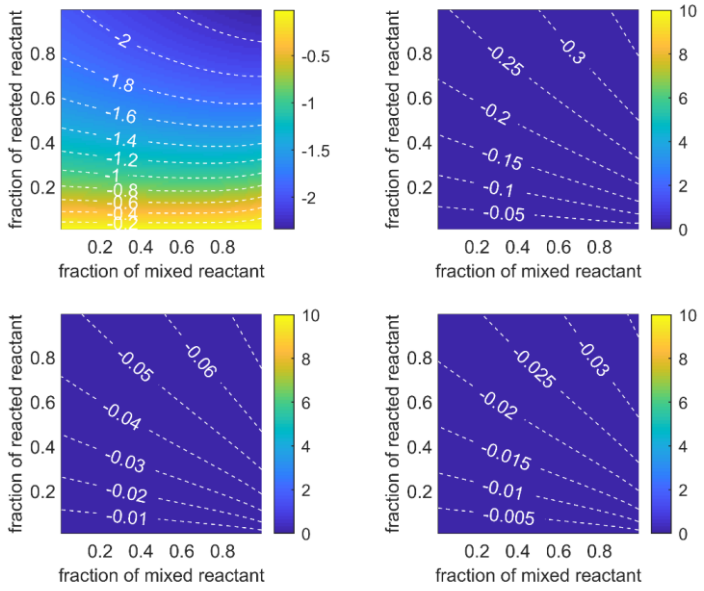

255

256 **Figure S3.** Simulation deviation of the isotopic composition of the product for varying

设置了格式: 字体颜色: 黑色

带格式的: 周围环绕

sub-steps (a) 1, (b) 10, (c) 50, and (d) 100, relative to reference simulation with 1000 sub-steps. Each simulation involves the addition of a compound with an initial δ-value of 10.0‰ to the substrate (initially δ = 0‰), while the chemical reaction exhibits an isotopic effect with a fractionation factor of α= 1.0167. The fractions of added and removed products range from 1% to 99% of the initial amount of substrate and are uniformly divided at every time sub-step. The color scheme and contour lines illustrate the δ-value differences between the respective simulations and the referenced simulation.

带格式的: 周围环绕

References

National Centers for Environmental Prediction/National Weather Service/NOAA/U.S. Department of Commerce, NCEP GDAS/FNL 0.25 Degree Global Tropospheric Analyses and Forecast Grids, Research Data Archive at the National Center for Atmospheric Research, Computational and Information Systems Laboratory, 2015, updated daily, DOI: 10.5065/D65Q4T4Z (accessed 2022/12/5),

Athanasopoulou, E., Tombrou, M., Pandis, S., and Russell, A.: The role of sea-salt emissions and heterogeneous chemistry in the air quality of polluted coastal areas, Atmos. Chem. Phys., 8, 5755-5769, 2008.

Bai, L. and Wang, Z.-L.: Anthropogenic influence on rainwater in the Xi'an City, Northwest China: Constraints from sulfur isotope and trace elements analyses, Journal of Geochemical Exploration, 137, 65-72, 10.1016/j.gexplo.2013.11.011, 2014.

Chen, S. L., Guo, Z. Y., Guo, Z. B., Guo, Q. J., Zhang, Y. L., Zhu, B., and Zhang, H. X.: Sulfur isotopic fractionation and its implication: Sulfate formation in $PM_{2.5}$ and coal combustion under different conditions, Atmospheric Research, 194, 142-149, 10.1016/j.atmosres.2017.04.034, 2017.

Cheng, Y., Zheng, G., Wei, C., Mu, Q., Zheng, B., Wang, Z., Gao, M., Zhang, Q., He, K., and Carmichael, G.: Reactive nitrogen chemistry in aerosol water as a source of sulfate during haze events in China, Sci. Adv., 2, e1601530, 2016.

Ding, S., Chen, Y., Li, Q., and Li, X.-D.: Using Stable Sulfur Isotope to Trace Sulfur Oxidation Pathways during the Winter of 2017–2019 in Tianjin, North China, International Journal of Environmental Research and Public Health, 19, 10966, 2022.

Fan, M.-Y., Zhang, Y.-L., Lin, Y.-C., Li, J., Cheng, H., An, N., Sun, Y., Qiu, Y., Cao, F., and Fu, P.: Roles of sulfur oxidation pathways in the variability in stable sulfur isotopic composition of sulfate aerosols at an urban site in Beijing, China, Environ. Sci. Technol. Lett., 7, 883-888, 2020.

Fountoukis, C. and Nenes, A.: ISORROPIA II: a computationally efficient thermodynamic

带格式的: 周围环绕

equilibrium model for K^+–Ca^{2+}–Mg^{2+}–NH_4^+–Na^+–SO_4^{2-}–NO_3^-–Cl^-–H_2O aerosols, Atmos. Chem. Phys., 7, 4639-4659, 2007.

Han, X., Lang, Y., Guo, Q., Li, X., Ding, H., and Li, S.: Enhanced Oxidation of SO2 by H2O2 During Haze Events: Constraints From Sulfur Isotopes, Journal of Geophysical Research: Atmospheres, 127, e2022JD036960, 2022.

Han, X., Guo, Q., Liu, C., Fu, P., Strauss, H., Yang, J., Hu, J., Wei, L., Ren, H., and Peters, M.: Using stable isotopes to trace sources and formation processes of sulfate aerosols from Beijing, China, Sci. Rep., 6, 2016a.

Han, X., Guo, Q., Liu, C., Strauss, H., Yang, J., Hu, J., Wei, R., Tian, L., Kong, J., and Peters, M.: Effect of the pollution control measures on $PM_{2.5}$ during the 2015 China Victory Day Parade: Implication from water-soluble ions and sulfur isotope, Environ. Pollut., 218, 230-241, 2016b.

Hong, S.-Y., Dudhia, J., and Chen, S.-H.: A revised approach to ice microphysical processes for the bulk parameterization of clouds and precipitation, Monthly weather review, 132, 103-120, 2004.

Hong, S.-Y., Noh, Y., and Dudhia, J.: A new vertical diffusion package with an explicit treatment of entrainment processes, Monthly weather review, 134, 2318-2341, 2006.

Hong, Y., Zhang, H., and Zhu, Y.: Sulfur isotopic characteristics of coal in China and sulfur isotopic fractionation during coal-burning process, Chinese Journal of Geochemistry, 12, 51-59, 1993.

Janssens-Maenhout, G., Crippa, M., Guizzardi, D., Dentener, F., Muntean, M., Pouliot, G., Keating, T., Zhang, Q., Kurokawa, J., and Wankmüller, R.: HTAP_v2. 2: a mosaic of regional and global emission grid maps for 2008 and 2010 to study hemispheric transport of air pollution, Atmos. Chem. Phys., 15, 11411-11432, 2015.

Kain, J. S.: The Kain–Fritsch Convective Parameterization: An Update. , Journal of Applied Meteorology and Climatology, 43, 170–181 2004.

Li, J., Zhang, Y.-L., Cao, F., Zhang, W., Fan, M., Lee, X., and Michalski, G.: Stable sulfur isotopes revealed a major role of transition-metal ion-catalyzed SO_2 oxidation in haze episodes,

带格式的: 周围环绕

Environ. Sci. Technol., 54, 2626-2634, 2020.

Li, M., Zhang, Q., Kurokawa, J.-i., Woo, J.-H., He, K., Lu, Z., Ohara, T., Song, Y., Streets, D. G., and Carmichael, G. R.: MIX: a mosaic Asian anthropogenic emission inventory under the international collaboration framework of the MICS-Asia and HTAP, Atmos. Chem. Phys., 17, 935-963, 2017.

Lin, M., Zhang, X., Li, M., Xu, Y., Zhang, Z., Tao, J., Su, B., Liu, L., Y., S., and Thiemens, M. H.: Five-S-isotope evidence of two distinct mass-independent sulfur isotope effects and implications for the modern and Archean atmospheres, PNAS, 115, 8541-8546, 2018.

Lin, Y.-C., Yu, M., Xie, F., and Zhang, Y.: Anthropogenic emission sources of sulfate aerosols in Hangzhou, East China: insights from isotope techniques with consideration of fractionation effects between gas-to-particle transformations, Environ. Sci. Technol., 56, 3905-3914, 2022.

Maruyama, T., Ohizumi, T., Taneoka, Y., Minami, N., Fukuzaki, N., Mukai, H., Murano, K., and Kusakabe, M.: Sulfur isotope ratios of coals and oils used in China and Japan, Nippon Kagaku Kaishi, 45-51, 10.1246/nikkashi.2000.45, 2000.

Monin, A. and Obukhov, A.: Osnovnye zakonomernosti turbulentnogo peremeshivanija v prizemnom sloe atmosfery (Basic laws of turbulent mixing in the atmosphere near the ground), Trudy geofiz. inst. AN SSSR, 24, 163-187, 1954.

Mukai, H., Tanaka, A., Fujii, T., Zeng, Y. Q., Hong, Y. T., Tang, J., Guo, S., Xue, H. S., Sun, Z. L., Zhou, J. T., Xue, D. M., Zhao, J., Zhai, G. H., Gu, J. L., and Zhai, P. Y.: Regional characteristics of sulfur and lead isotope ratios in the atmosphere at several Chinese urban sites, Environ. Sci. Technol., 35, 1064-1071, 10.1021/es001399u, 2001.

Ohizumi, T., Fukuzaki, N., and Kusakabe, M.: Sulfur isotopic view on the sources of sulfur in atmospheric fallout along the coast of the Sea of Japan, Atmos. Environ., 31, 1339-1348, 10.1016/s1352-2310(96)00278-6, 1997.

Pincus, R., Barker, H. W., and Morcrette, J. J.: A fast, flexible, approximate technique for computing radiative transfer in inhomogeneous cloud fields, Journal of Geophysical Research: Atmospheres, 108, 2003.

带格式的: 周围环绕

Song, S., Gao, M., Xu, W., Shao, J., Shi, G., Wang, S., Wang, Y., Sun, Y., and McElroy, M. B.: Fine-particle pH for Beijing winter haze as inferred from different thermodynamic equilibrium models, Atmos. Chem. Phys., 18, 7423-7438, 10.5194/acp-18-7423-2018, 2018.

Stockwell, W. R., Kirchner, F., Kuhn, M., and Seefeld, S.: A new mechanism for regional atmospheric chemistry modeling, Journal of Geophysical Research: Atmospheres, 102, 25847-25879, 1997.

Wang, Z., Akimoto, H., and Uno, I.: Neutralization of soil aerosol and its impact on the distribution of acid rain over east Asia: Observations and model results, Journal of Geophysical Research: Atmospheres, 107, ACH 6-1-ACH 6-12, 2002.

Wang, Z., Ueda, H., and Huang, M.: A deflation module for use in modeling long-range transport of yellow sand over East Asia, Journal of Geophysical Research: Atmospheres, 105, 26947-26959, 2000.

Wei, L., Yue, S., Zhao, W., Yang, W., Zhang, Y., Ren, L., Han, X., Guo, Q., Sun, Y., Wang, Z., and Fu, P.: Stable sulfur isotope ratios and chemical compositions of fine aerosols ($PM_{2.5}$) in Beijing, China, Sci. Total Environ., 633, 1156-1164, 10.1016/j.scitotenv.2018.03.153, 2018.

Wei, Y., Chen, X., Chen, H., Li, J., Wang, Z., Yang, W., Ge, B., Du, H., Hao, J., and Wang, W.: IAP-AACM v1. 0: a global to regional evaluation of the atmospheric chemistry model in CAS-ESM, Atmos. Chem. Phys., 19, 8269-8296, 2019.

Wu, Q. X. and Han, G. L.: Sulfur isotope and chemical composition of the rainwater at the Three Gorges Reservoir, Atmospheric Research, 155, 130-140, 10.1016/j.atmosres.2014.11.020, 2015.

Xiao, H.-Y. and Liu, C.-Q.: The elemental and isotopic composition of sulfur and nitrogen in Chinese coals, Organic Geochemistry, 42, 84-93, 10.1016/j.orggeochem.2010.10.011, 2011.

Xiao, H.-Y., Tang, C.-G., Xiao, H.-W., Liu, X.-Y., and Liu, C.-Q.: Identifying the change in atmospheric sulfur sources in China using isotopic ratios in mosses, J. Geophys. Res-Atmos., 114, 10.1029/2009jd012034, 2009.

Xiao, H. W., Xiao, H. Y., Long, A. M., Wang, Y. L., and Liu, C. Q.: Sources and

带格式的: 周围环绕

meteorological factors that control seasonal variation of delta S-34 values in rainwater, Atmospheric Research, 149, 154-165, 10.1016/j.atmosres.2014.06.003, 2014.

Zaveri, R. A. and Peters, L. K.: A new lumped structure photochemical mechanism for large-scale applications, Journal of Geophysical Research: Atmospheres, 104, 30387-30415, 1999.

Zhang, L., Brook, J. R., and Vet, R.: A revised parameterization for gaseous dry deposition in air-quality models, Atmos. Chem. Phys., 3, 2067-2082, 2003.

Zheng, M., Song, D., Zhang, D., and Zhao, Z.: Variability of sulfur and oxygen isotope values within wet precipitation and its correlation with diminished anthropogenic sulfur dioxide (SO_2) emission, Atmos. Environ., 317, 120185, 2024.

Zhu, G., Guo, Q., Chen, T., Lang, Y., Peters, M., Tian, L., Zhang, H., and Wang, C.: Chemical and sulfur isotopic composition of precipitation in Beijing, China, Environmental Science and Pollution Research, 23, 5507-5515, 10.1007/s11356-015-5746-2, 2016.

带格式的: 周围环绕